NASA-CR-198972

IN-02-CR

5943

P-41

MCAT Institute
Final Report
95-09

ORIGINAL CONTAINS
COLOR ILLUSTRATIONS

Control of Unsteady Separated Flow Associated With the Dynamic Stall of Airfoils

M. C. Wilder

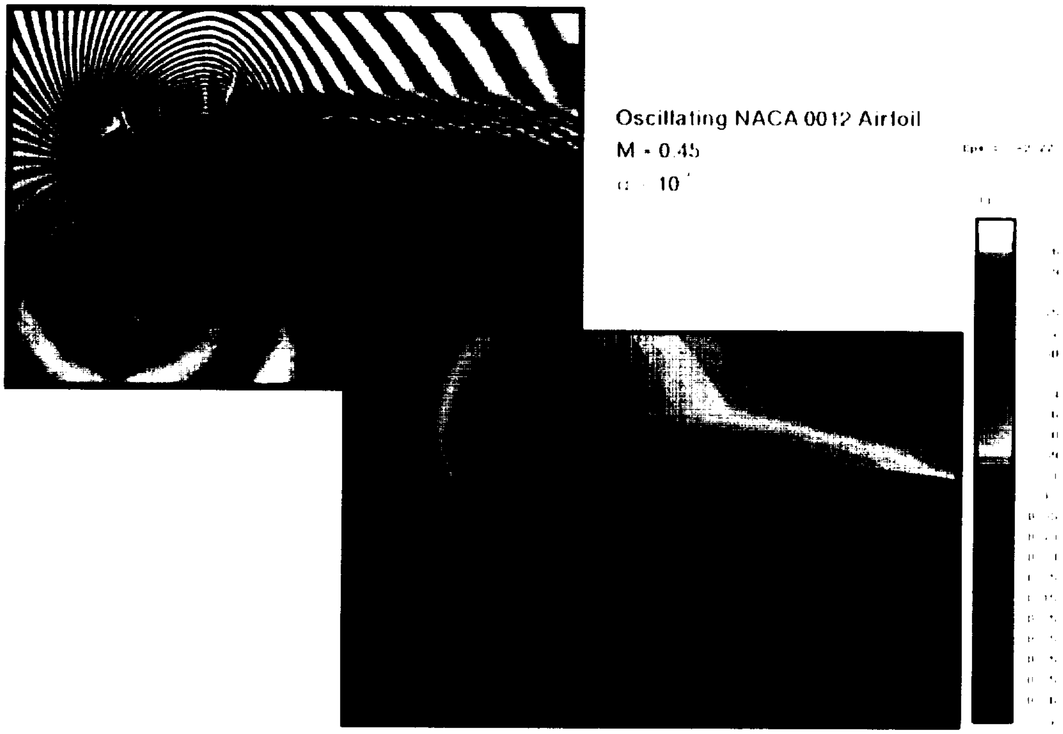

January 1995

MCAT Institute
3933 Blue Gum Drive
San Jose, CA 95127

(NASA-CR-198972) CONTROL OF
UNSTEADY SEPARATED FLOW ASSOCIATED
WITH THE DYNAMIC STALL OF AIRFOILS
Final Report (MCAT Inst.) 41 p

N95-32193

Unclas

63/02 0058485

Final Report for Cooperative Agreement No. NCC2-637
31 January 1995

Control of Unsteady Separated Flow Associated With the Dynamic Stall of Airfoils

M. C. Wilder
MCAT Institute, San Jose, CA 95127

Abstract

An effort to understand and control the unsteady separated flow associated with the dynamic stall of airfoils was funded for three years through the NASA cooperative agreement program. As part of this effort a substantial data base was compiled detailing the effects various parameters have on the development of the dynamic stall flow field. Parameters studied include Mach number, pitch rate, and pitch history, as well as Reynolds number (through two different model chord lengths) and the condition of the boundary layer at the leading edge of the airfoil (through application of surface roughness).

It was found for free stream Mach numbers as low as 0.4 that a region of supersonic flow forms on the leading edge of the suction surface of the airfoil at moderate angles of attack. The shocks which form in this supersonic region induce boundary-layer separation and advance the dynamic stall process. Under such conditions a super critical airfoil profile is called for to produce a flow field having a weaker leading-edge pressure gradient and no leading-edge shocks. An airfoil having an adaptive-geometry, or Dynamically Deformable Leading Edge (DDLE), is under development as a unique active flow-control device. The DDLE, formed of carbonfiber composite and fiberglass, can be flexed between a NACA 0012 profile and a supercritical profile in a controllable fashion while the airfoil is executing an angle-of-attack pitch-up maneuver.

The Dynamic stall data were recorded using Point Diffraction Interferometry (PDI), a noninvasive measurement technique. A new high-speed cinematography system was developed for recording interferometric images. The system is capable of phase-locking with the pitching airfoil motion for real-time documentation of the development of the dynamic stall flow field. Computer-aided image analysis algorithms were developed for fast and accurate reduction of the images, improving interpretation of the results.

Table of Contents

Nomenclature

C_p	pressure coefficient
$C_p{}^*$	critical pressure coefficient
c	airfoil chord
f	oscillation frequency, Hz
k	reduced frequency, $\frac{\pi f c}{U_\infty}$
L	test section span
M	free stream Mach number
n	index of refraction
Re	Reynolds number based on c and U_∞
t	time, seconds
U_∞	free stream velocity
x,y	chordwise and vertical distance; model-fixed coordinate system with origin located at leading edge of the airfoil
x′,y′	horizontal and vertical distance; tunnel-fixed coordinate system with origin located at leading edge of the airfoil for $\alpha = 0^0$
α	angle of attack
α_0	mean angle of attack
α_m	amplitude of oscillating motion
$\dot{\alpha}$	pitch rate in deg/sec
α^+	nondimensional pitch rate, $\frac{\dot{\alpha} c}{U_\infty}$
λ_0	wavelength of laser light (532 nm)
γ	ratio of specific heats
ϵ	fringe number
ρ	density
ρ_r	density at reference (atmospheric) conditions

I. Introduction

The maneuverability of many modern aircraft is limited by the prospect of such unsteady separated flow phenomena as flutter and dynamic stall. Dynamic stall is the expression given to describe the stall process of an aerodynamic surface subjected to forced unsteadiness. Specific examples include stall of the retreating blade of a helicopter rotor in forward flight, and stall of the wing on an aircraft executing a rapid pitch-up maneuver. For a helicopter in forward flight, the retreating blade is moving slower, relative to the free stream, than the advancing blade by an amount equal to the forward speed of the helicopter. To compensate for the asymmetric lift across the rotor that this situation would produce, the retreating blade is pitched to a higher angle of attack, relative to the advancing blade. When an airfoil is pitched up rapidly, there exists a phase lag in the development of the lift (suction pressure). Consequently, the flow will remain attached at angles exceeding the angle of steady stall.

Lift augmentation and stall delay are two advantageous qualities of dynamic stall flow.

Detrimental aspects of dynamic stall arise following flow separation. Not only is the lift lost, as in steady flow stall, but the coalescing and convecting downstream of shed vorticity produces intense fluctuations of the pitching moment on the airfoil. Moment fluctuations sever enough to cause structural damage can occur on aircraft experiencing dynamic stall.

A challenging problem to aerodynamicists is to control unsteady flow separation phenomena like dynamic stall, so that the desirable attributes can be exploited while the detrimental side effects can be mitigated. To control dynamic stall will first require a richer understanding of the governing parameters which shape the flow development.

The development of a dynamic-stall flow is dependent on numerous parameters which include the Mach and Reynolds numbers of the flow, the profile of the airfoil, the pitch rate and pitch history of the airfoil, and the state of the boundary layer on the airfoil. Compressibility effects, for example, have been shown [1] to be significant even for flows having a moderate free stream Mach number of M = 0.2. Compressibility influences the flow development in two ways: by lessening the degree of lift augmentation observed, and by advancing the stall angle. As a consequence, the higher the free stream Mach number, the shorter the time available to exploit the advantageous effects of dynamic stall. For flows at high free stream Mach number, the formation of supersonic regions of flow on the airfoil surface can give rise to shock induced separation, further advancing of stall. Moreover, the very nature of the stall process can be altered by flow compressibility. Carr et al [2] demonstrated that dynamic stall of an oscillating NACA 0012 airfoil changes from a trailing-edge stall to a leading-edge stall when compressibility effects become significant. Conversely, it was also shown that a supercritical airfoil, the NLR-7301, exhibited trailing-edge stall in both compressible and incompressible flows.

With these observations in mind, an adaptive geometry airfoil was proposed as a dynamic stall flow control device [3]. Returning again to the example of a helicopter, such an airfoil would have a high-speed profile while on the advancing side of the rotor, then alter to a supercritical profile while on the retreating side. The profile change must occur on a time scale of milliseconds. The challenge is to find a surface material flexible enough to achieve the response time required, yet rigid enough to deform repeatedly, in a controlled fashion, under rapidly varying aerodynamic loads. Previous attempts at active flow control have relied on devices which force local unsteadiness in the flow (i.e., oscillating flaps of suction/blowing) [4-6]. Such experiments have chiefly been performed at low Mach numbers and under steady flow conditions.

This report will describe the efforts to develop an adaptive geometry airfoil. Also discussed in this report are the important results of a continuing effort to document the influence of various parameters on the dynamic stall of pitching airfoils. In the course of this work, valuable advances were made in flow diagnostic instrumentation and image/data analysis techniques. These advances will be highlighted.

II. The Experimental Facilities and Techniques

The dynamic stall experiments were conducted in the Compressible Dynamic Stall Facility (CDSF) [7] in the Fluid Mechanics Laboratory (FML) of NASA Ames Research

Center. The tunnel is part of the in-draft wind tunnel complex at the FML and had a 25cm x 35cm rectangular test section following a 3:1 three-dimensional contraction. A variable area choked throat located downstream of the test section provided control of the flow rate in the test section over the Mach number range $0 \leq M \leq 0.5$. The choked throat also isolated the test section from downstream disturbances by locating a normal shock within the throat.

A. Experimental Conditions

Compressible dynamic stall flow depends on a large parameter space and the effects on the flow of a variety of these parameters was investigated. Experiments were conducted at free stream Mach numbers spanning the range of $0.2 \leq M \leq 0.45$ for two symmetric airfoils (NACA 0012) of differing chord lengths. The first airfoil was 7.62 cm (3 in.) in chord, giving a chord Reynolds number range of $0.36x10^6 \leq Re \leq 0.9x10^6$ for the Mach number range investigated. The chord length of the second airfoil was 15.24 cm (6 in.) with the corresponding Reynolds number range of $0.72x10^6 \leq Re \leq 1.8x10^6$. This model was instrumented with ten surface pressure taps. Pressure measurements were made under steady flow conditions and used to validate the interpretation of interferometry data. The interferometry technique will be described later.

Optical quality glass windows mounted in circular frames on either side of the test section, and capable of rotating, supported the airfoil model. The quarter-chord point of the airfoil was located at the center of the circular window frames. For the experiments reported here, the airfoil was maneuvered through one of two pitch schedules, for a range of pitch rates. The two different pitch schedules were generated with interchangeable drive mechanisms; one for sinusoidally oscillating the airfoil [7] and the other for producing a linear variation of the angle of attack over a single pitch-up [8]. These drives, respectively sketched in Fig. 1a and 1b, were mounted on top of the test section and were linked to the window frames. An 800 count/revolution optical encoder was attached to either drive for monitoring the instantaneous angle of attack of the airfoil.

The oscillatory pitch schedule was of the form

$$\alpha(t) = \alpha_0 - \alpha_m sin\ 2\pi ft.$$

The mean angle of attack was set to $\alpha_0 = 10^0$ and the amplitude of oscillation was $\alpha_m = 10^0$. Oscillation frequencies up to $f = 54$Hz were used giving a reduced frequency range of $0 \leq k \leq 0.15$.

In the case of the linear schedule, the maneuver consisted of a single (or transient) pitch-up, rapidly taking the model from $\alpha = 0^0$ to $\alpha = 60^0$. Pitch rates up to 3600^0/sec were possible, giving a nondimensional pitch rate range of $0 \leq \alpha^+ \leq 0.04$.

The Mach numbers of the flows investigated were comparable to flight Mach numbers, although the Reynolds numbers were several times lower than those observed on aircraft in flight. In order to simulate higher Reynolds number flows additional experiments were performed wherein boundary-layer tripping devices were attached along the leading edge of the airfoils. Constructing a boundary-layer trip that would produce the required effects over the entire range of flow conditions studied proved challenging. An empirical approach was followed in which the effects of five different configurations of distributed roughness elements were studied. As a result, a wealth of data on the effects of boundary-layer tripping on dynamic stall was compiled. Details on the materials and physical dimensions of the trips will be provided later in this report.

The combinations of all these parameters for which data were acquired are listed in Tables 1-3.

B. Boundary Layer Trips

A review of literature [9,10] was conducted to obtain the first estimate of the required trip size. The leading-edge-stalling NACA 0012 airfoil flow bears considerable qualitative similarity to the flow over a circular cylinder. Therefore, it was decided to use a roughness strip as the tripping device following the recommendations of Nakamura and Tomonari [9]. A formula given in Ref. 12 was used to determine the minimum size of the trip for the boundary layer. As reported by Wider et al [11], this formula indicated a grit size diameter of 56 - 89μm (0.0022 - 0.0035in.) for $0.2 \leq M \leq 0.3$. Boundary layer transition trips were formed by bonding three-dimensional roughness elements in a span-wise strip of height 170μm along the surface of the airfoil. Wind tunnel tests were performed with this trip in place. The results indicated premature stall [11], attributable to the large trip height resulting from the fabrication process used. Thus, it became necessary to conduct a systematic investigation of different trip heights to identify a trip that yielded acceptable results. A total of five trip configurations with the following characteristics were tested:

Trip 1. 74 - 89 μm diameter carborundum grains (number 220 polishing grit) were bonded to the airfoil surface using a water-soluble-adhesive (Polaroid print-coating material). The strip was located on the upper surface for $0.005 \leq x/c \leq 0.03$. The average height of the trip was 170 μm.

Trip 2. A repeat of trip number 1 using a spray-on enamel lacquer adhesive. The average height of this trip was 100 μm. The lacquer was used for all subsequent trips.

Trip 3. Made of the same materials as trip number 2, this strip covered the entire leading edge starting on the lower surface at $x/c = 0.05$ (near the mean stagnation point) and extending to the upper surface at $x/c = 0.03$. The average height was approximately 130 μm.

Trip 4. A smaller grit material, 22 - 36 μm aluminum oxide particles, was used for trips 4 and 5. Trip number 4 was located on the upper surface, $0.005 \leq x/c \leq 0.03$, like trips 1 and 2. The trip was estimated to be no higher than 43 μm.

Trip 5. The last trip extended from $x/c = 0.05$ on the lower surface around the leading edge to $x/c = 0.05$ on the upper surface. The trip height was approximately 40 - 50 μm.

The trip heights were estimated from digitized images of the silhouette of the airfoil by magnifying and scaling the images on an IRIS workstation. The uncertainty in the estimated trip heights is $\pm 10\mu m$. The boundary layer height was estimated to be about 60μm at the point of flow separation ($x/c = 0.02$ to 0.04).

C. Optical Measurement Techniques

Due to the highly unsteady nature of the development of dynamic stall, a nonintrusive technique was employed to capture the details of the flow. Surface pressure measurements were also made under steady flow conditions and the results were used to confirm the sufficiency of the assumptions made when interpreting interferometric images to yield pressure values.

1. *Stroboscopic Point Diffraction Interferometry*

Stroboscopic point diffraction interferometry (PDI) [12,13] was employed in both oscillating airfoil and transiently pitching airfoil studies. The PDI technique produces instantaneous images of the fluid density field around the airfoil in the form of interference fringe patterns. Each fringe represents a line of constant density (averaged across the test section span), and through image analysis techniques and the application of the appropriate gas dynamical relations, quantified global and surface pressure distributions can be extracted from the images. This ability coupled with the nonintrusive nature of PDI makes it an invaluable tool in the investigation of the rapidly developing dynamic stall flow field.

The light source was a CW/pumped Nd:YAG laser, frequency doubled to 532nm wavelength, and capable of pulsing at rates up to 50kHz. The laser was externally triggered with no measurable delay between issuing the trigger and detecting the light pulse. The trigger could be supplied manually (during steady flow experiments) or automatically by custom built instrumentation. This instrumentation would provide a single pulse of the laser when the airfoil instantaneously reached a preset angle of attack within its pitch schedule. The duration of the light pulse and the energy of the beam varied nonlinearly with the pulse rate, with values of 85ns/140μJ at 500Hz, 420ns/25μJ at 40kHz, and 100ns/11μJ at 50kHz. The optical arrangement of the PDI system was similar to a Schlieren system (see Fig. 2). The laser beam was expanded with a negative lens then directed by a spherical Schlieren mirror through the test section. The lens and mirror were arranged so that the expanded beam appears as a parallel light source (source at infinity) with rays parallel to the span of the airfoil model. The expanded beam was large enough to illuminate the entire window to the test section (6 in. diameter). On the opposite side of the test section a second spherical Schlieren mirror, having the same focal length as the first mirror, focused the transmitted light to a point off the optical axis of the expanded beam. The 'Z-angle' of the system was kept small to reduce aberration. A neutral density filter was located at this focal plane such that a pin-hole in the filter was positioned at the point where the light would focus when there was no flow in the test section. (In practice, the pin-hole was created *in situ* by burning a hole through the filter with the focused laser beam.) During an experiment, the light which passed through the pin-hole acted as the reference beam for producing the interference. Light which passed around the pin-hole had been phase-shifted (and deflected) due to the density variations across the test section. As the Mach number of the flow increases, the amount of light deflected from the pin-hole also increases. This results in a weaker reference beam and a stronger signal beam, and the interference fringes become less visible. To counter this problem, filters ranging in neutral density from 0.8 to 1.5 were used. Finally, a system of imaging lenses focused the interference pattern formed at the pin-hole onto the film plane of a camera. Interferograms were recorded on Polaroid Type 57 film or Kodak T-MAX 400 35mm film, depending on the camera used. The photographs were then digitized, using a scanning digitizer, for subsequent analysis. The spatial resolution of the digitizer was 300 dpi (dots per inch) and the color resolution was 8 bits (256 shades).

2. Determination of Pressure Coefficient

For a standard interferometer, the path length difference $\overline{\Delta PL}$ due to density (or phase) changes can be related to the fringe number ϵ as,

$$\epsilon = \frac{\overline{\Delta PL}}{\lambda_0} = \frac{1}{\lambda_0}\int (n - n_r)dz$$

where n is the refractive index in the signal beam, n_r is that in the reference beam and λ_0 is the wave length of the light used.

For a two-dimensional flow, the above equation can be simplified to,

$$\epsilon = (n - n_r)\frac{L}{\lambda_0}$$

where L is the test section span. If ϵ is an integer, then the fringe is bright and if it is a half integer, the fringe is dark. Using the Gladstone - Dale equation [14] and the perfect gas equation, the above equation can be reduced to,

$$\rho - \rho_r = (\frac{\lambda_0}{n_0 - 1})(\frac{\epsilon\rho_0}{L}) = A\epsilon$$

Since λ_0 = 532 nm, L = 25cm, $(n_0 - 1) = 2.733 \text{ x } 10^{-4}$ for air and $\rho_0 = 1.21 kg/m^3$, for the present experiments,

$$\rho - \rho_r = A\epsilon = 0.009421\epsilon$$

or

$$\frac{\rho}{\rho_0} = \frac{\rho_r}{\rho_0} + \frac{A\epsilon}{\rho_0}$$

Since $\frac{\rho_r}{\rho_0}$ is a function of the free stream Mach number only, $\frac{\rho}{\rho_0}$ can be determined by knowing the fringe number. Note that in this method, a positive fringe number represents deceleration and vice versa. Hence, fringes from the free stream to the stagnation point have positive values. The corresponding pressure along a fringe was derived using isentropic flow relations as:

$$C_p = \frac{\left[(\frac{\rho}{\rho_r})^\gamma - 1\right]}{\left[\frac{\gamma}{2}M^2\right]}.$$

D. Surface Pressure Measurement Techniques

Average surface pressures were recorded for steady flow over the 15.24cm (6 inch) chord length NACA 0012 airfoil model. For each measurement a reference pressure, the ambient atmospheric pressure, and the pressure at ten surface taps along the airfoil chord were recorded using a single transducer coupled to a Scanivalve. The reference pressure and the ambient atmospheric pressure were also recorded with two calibrated Paroscientific pressure transducers, thus providing online calibration of the Scanivalve measurements. These measurements were then used to verify the data reduction technique applied to the PDI images.

E. High-Speed Imaging Instrumentation

The dynamic stall flow field becomes highly non-linear at the time of boundary-layer separation and dynamic-stall vortex formation. Consequently, the flow field is not perfectly repeatable from cycle to cycle. A system was developed for photographically recording interferometric images at very high rates (up to 40,000 images/sec). With this system the development of the dynamic stall flow can be imaged in detail over a single pitching maneuver, thus eliminating unwanted cycle-to-cycle variations from the data. The system was further needed to record the shape history of the dynamically deformable leading edge.

1. Image Conversion Camera System

Photons incident on the image conversion tube of the IMACON camera are converted into a stream of electrons, which is steered and gated by two pair of high-voltage plates to form images on a phosphor screen. Plug-in modules provide gating rates from $2.5 \mathrm{x} 10^5$Hz up to 10^7Hz. Using the $2.5 \mathrm{x} 10^5$Hz gate rate up to twelve images can be recorded on a sheet of Polaroid Type 107 film (3in x 5in sheet, ASA 3600). The framing sequence can be initiated with a 10 volt - 200 volt trigger pulse, however, there is a $20 \mu s$ to $200 \mu s$ delay between receiving the trigger pulse and the first frame. This unknown delay makes synchronizing the camera with a pulsed laser light source (light pulses ¡ 500ns in duration) extremely difficult. Instead, the IMACON was used with a continuous light source and only for recording the shape history of the DDLE models. These measurements were reported by Wilder [15].

2. Drum Camera System

A new phase-locked, high-speed photographic recording system was developed for use with the PDI technique [16], which employs a Cordin Dynafax Model 350 drum camera. The camera records up to 224 16mm-size frames, in two rows, along a strip of standard 35mm film at rates up to 40,000 frames/sec. The film strip is held on the inside surface of a rapidly rotating drum within the camera. Light entering the camera lens is directed to a rotating multifaceted mirror. Light reflected from the mirror facets sweeps past a frame window to fall on the film. The mirror and the drum rotate such that the relative motion of the film and the light is canceled. There are two frame windows which form two rows of 16mm images along a strip of 35mm film. The images alternate between the two rows and the second row is displaced by sixteen frames from the first. A maximum of 224 images can be recorded on each film strip, although only 200 images are recorded here to allow unambiguous identification of the first frame.

Custom designed instrumentation provided phase-locking of the pulsed laser light source with the "frame events" of the drum camera. Here, "frame event" means the instant at which a mirror facet is aligned with a frame window. The instrumentation also simultaneously records the position of the angle-of-attack encoder and stores the data in a FIFO memory buffer for later retrieval. The instrumentation receives a pulse from an infrared optical trigger (light emitting diode (LED)/photodetector pair) located inside the camera upon each passage of a mirror facet, and then emits a pair of pulses (with suitable time delays) which fire the laser. The time delays are pre-tuned so that the laser fires at the instant of a frame event; one laser pulse for each of the two frame windows. Tuning is accomplished by placing photodetectors in the frame windows and adjusting the time delays to maximize the intensity of the laser light detected. The system must be re-tuned if the frame rate is changed. A block diagram illustrating the system is shown in Fig. 3.

Sequences of 200 images have been obtained at frame rates of 11,560 frames/sec and 20,000 frames/sec for an oscillating airfoil at M = 0.3 and M = 0.45 at a reduced frequency of k = 0.05. Data for M = 0.3, k = 0.05 and 11,560 frames/sec were reported by Chandrasekhara et al [16]. At these conditions, the dynamic stall was imaged over a single oscillation cycle with an average resolution of 0.07 degrees/image.

III. Discussion of Results

A. Flow Control Device Designs

1. Adaptive-Geometry Bench Test Models

Two design approaches have been pursued in developing the adaptive-geometry airfoil. The first approach employed a material that uses electromagnetic repulsive force to change shape. This material was originally designed to forcefully expel ice build-up from the leading-edge of aircraft wings [17]. The material is simply a helical, or coil shaped conductive ribbon embedded in a non-conductive substrate, with the helix flattened. An elastic skin holds the flattened helix to the airfoil surface. The electromagnetic forces that result when a high-voltage pulse is sent through the ribbon cause the helix to open, and the elastic skin returns the surface to its original shape when the electromagnetic forces have subsided. The high-voltage pulse was generated by discharging a capacitor through the coil. Voltages as high as 1000 volts were used. The device is sketched in Fig. 4. A reflective grid on the model was used to measure the instantaneous shape of the surface. The grid was imaged using the image conversion camera system, described previously, then digitized. Shape histories of the rapidly deforming leading-edge profile for several models were reported by Wilder [15, 18]. An example frame is shown in Fig. 4. This plot shows the undeformed surface (dotted line) and the shape of the surface 2.2ms after the pulse (solid line). The response time for this device was sufficient, although the leading edge proved too flexible to withstand the expected aerodynamic loads.

A more rigid, composite material skin, which is deformed by mechanical force was used in the second design approach to the adaptive-geometry airfoil. A bench-test model comprising the upper surface of the leading 25% chord of a five times over-sized (760 mm chord) airfoil was built. The skin was molded in the shape of the "deformed" surface, and an applied load forces the skin into the shape of the neutral airfoil (NACA 0012). Releasing the load allowed the skin to return to its original shape. Results of the bench tests were reported by Wilder [18].

2. Adaptive-Geometry Wind Tunnel Test Model

A wind tunnel test model was developed from the bench-test design described in the preceding section. The trailing 80% of this model has an NACA 0012 profile and is supported in the wind tunnel by the same mount used by the 15.24cm-chord NACA 0012 model. The leading 20% is the DDLE and is comprised of a sliding push plate having a

NACA 0012 leading-edge profile, covered by a carbonfiber and fiberglass outer skin which has a circular leading-edge profile with a radius of curvature larger than that of the NACA 0012 (see Fig. 4). The push plate is connected to the skin at the leading edge. Computer-controlled actuators drive the push plate, and can be programmed for a range of motion schedules. An incremental encoder on the actuators provides feedback of the position of the push plate. The skin is flexible yet rigid enough to support the aerodynamic loads expected in the experiments. Sliding the push plate forward stretches the skin into the NACA 0012 profile. Tests of the model will begin soon.

B. Dynamic Stall Flow Field

1. *Parametric Effects on the Flow Field*

The gross features of the compressible dynamic stall flow field are the same for both the transiently pitching and the oscillating airfoils. Examples are presented for the oscillating airfoil case, while results from the transiently pitching airfoil can be found in Chandrasekhara et al [19,20] and Wilder et al [11]. A laminar separation bubble was observed to form on the suction surface of the leading edge of the airfoil for any pitch rate and for all Reynolds numbers investigated. The angle of attack at which the bubble formed and the extent of the separated region varied with both pitch rate and Mach number. The bubble formed later (at higher angles) with increasing pitch rate and earlier (at lower angles) with increasing Mach number. It was also observed by Chandrasekhara et al [20] that the dynamic stall vortex forms with the bursting of this separation bubble. The early stages of dynamic stall vortex development is captured in the sequence of images shown in Fig. 6. These images were taken for the flow conditions M = 0.3, k = 0.1 and at angles of attack of $\alpha = 10^0, 12^0, 13^0$, and 14^0 for Figs. 6a-6d, respectively. Referring to Fig. 6a, the semicircular fringe which begins and ends on the lower surface of the airfoil encloses the stagnation point of the flow. Similarly, the suction peak, located on the upper surface at approximately 1% of the chord, is enclosed by fringes which begin and end on this surface. The separation bubble is clearly present on the airfoil at these conditions, and ends at approximately 2% of the chord at the location where the fringes that are approaching the airfoil nearly normal to the surface abruptly turn tangent to the surface. With increasing angle of attack (Figs. 6b and 6c) the angle through which the fringes turn as approaching the airfoil surface is decreasing. This is evidence that the bubble is opening. By $\alpha = 14^0$ the imprint of the dynamic stall vortex is clearly seen as a wedge of fringes extending nearly vertical to the surface of the airfoil. Furthermore, the fringes in the outer flow are beginning to align parallel with the surface of the airfoil, which means the pressure there is equalizing along the surface (a fringe is an isobaric contour). The influence of the developing vortex prevents the flow from separating.

The peak suction pressure coefficient developed is plotted as a function of angle of attack in Fig. 7. For the conditions associated with Fig. 6 the suction pressure continues to grow, then hold steady until $\alpha > 14^0$, while M = 0.3 flow around a steady airfoil separated at $\alpha = 12^0$. This plot illustrates the delay of stall obtained with forced unsteadiness. The peak suction pressure coefficient attainable increases with pitch rate, but the pressure coefficient at any given angle of attack lags those corresponding to lower pitch rates. A similar result was reported in ref. 26 for M = 0.4 flow over a transiently pitching airfoil.

The delay in suction pressure development experienced with increasing forced unsteadiness extends to the entire surface pressure distribution. This effect in illustrated in Fig. 8 which shows the pressure distribution around the leading edge of the airfoil for M = 0.3; $\alpha = 10,^0$ and for three pitch rates: k = 0 (steady), k = 0.05, and k = 0.1. The downstream end of the separation bubble is seen in these data as an adverse pressure gradient between $0.01 \leq x/c \leq 0.02$.

A region of supersonic flow forms over the leading edge of the airfoil when the free stream Mach number is greater than 0.35 for the conditions studied. The formation of multiple shocks in the supersonic region was first reported from Schlieren investigations of dynamic stall of a transiently pitching airfoil [19]. An interferogram showing multiple lambda shocks over an oscillating airfoil is presented in Fig. 9. The flow conditions for this experiment were: M = 0.45; k = 0.05; $\alpha = 10^0$. The presence of multiple lambda shocks is further evidence that the flow is laminar over the leading edge (see reference [21]). Figure 10 is a quantized global pressure field determined from this image. The value of the pressure coefficient is given for several (highlighted) contour lines. The contour of critical pressure coefficient ($C_p{}^*$) is highlighted. The isentropic relations are increasingly invalid in the area inside this contour, where the flow experiences a series of compressions and expansions. However, the shocks are weak ($p_2/p_1 < 1.2$) and the data can be used for comparison with other, similarly obtained data.

The dependence of the flow on free stream Mach number (effect of compressibility) is illustrated in Fig. 11. This figure shows four interferograms (Figs. 11a-11d) taken with the airfoil at $\alpha = 12^0$, and oscillating at a reduced frequency of k = 0.05. In Fig. 11a, M = 0.3, a separation bubble is present on the upper surface of the leading edge. At M = 0.35 (Fig. 11b) the bubble has burst, and the dynamic stall vortex is beginning to coalesce. At higher Mach numbers (M = 0.4 and M = 0.45 for Figs. 11c and 11d, respectively) the imprint of the dynamic stall vortex is evident over a progressively larger region of the flow. This sequence of images illustrates the advancement of the dynamic stall phenomenon by fluid compressibility. Figures 11e-11f are color-coded pressure coefficient fields derived from an analysis of the images shown in Fig. 11a-11d. The critical pressure coefficient, $C_p{}^*$, is shown for each free stream Mach number. The color scales run from blue at stagnation to red at $C_p{}^*$, and through shades of pink up to white for increasing supersonic speed flows. The critical pressure coefficient is reached for all the conditions shown except for the M = 0.3 case (Fig. 11a and 11e). For the higher Mach number flows ($M \geq 0.4$) the formation of single and multiple shocks has been observed, as discussed above.

The final parametric study involved changing the Reynolds number while holding the Mach number constant by physically altering the chord length of the model. Oscillating and steady airfoil experiments were repeated for both untripped and tripped flow over a model having twice the chord length (see Table 3 for parameter spread). These resently acquired data are not yet fully analyzed and only some representative results are presented here. Surface pressure distributions for steady flow at $\alpha = 12^0$; M = 0.3 are shown for both airfoils in Fig. 12. The two curves shown for the 7.62cm chord airfoil ($Re = 0.6x10^6$) were derived from the analysis of PDI images. At this angle, the flow was bistable and could be either attached or stalled, depending on upstream disturbances. The higher

Reynolds number flow, Re = 1.2x10^6, remained attached until $\alpha = 13.4^0$, at which point a similar bistable condition occurred. The higher Reynolds number flow also developed a stronger suction pressure and showed a smaller separation bubble, though a bubble was still present for all conditions tested. The PDI images of the higher Re data have yet to be fully analyzed. The higher Re data presented in Fig. 12 were measured via surface pressure taps on the airfoil. Only ten taps were available, hence the lack of resolution across the stagnation region of the data.

The shocks which form for the M = 0.45 flows are significantly altered by increasing the Reynolds number, as is shown in Fig. 13. Both images are for the conditions M = 0.45; k = 0.05; and $\alpha = 10^0$ (Fig. 13a is an enlargement from Fig. 9). There were fewer compressions/expansions at the higher Re and the shocks were stronger, with p_2/p_1 approaching or exceeding a value of 1.4 (see Fig. 13b).

2. Effects of Boundary Layer Tripping

Boundary layer tripping in scale model tests is a traditional method for achieving Reynolds number similarity with full scale. Guidelines for developing a suitable trip, however, are based on steady flow conditions and may not suffice for a large amplitude unsteady flow such as dynamic stall. The facts that the dynamic stall vortex begins to coalesce very near the location of the suction peak (x/c ~ 0.02), and that the initiation of dynamic stall varies with pitch rate and free stream Mach number further complicate designing the trip. The "optimum" trip was found empirically by performing test using the five different trips described previously. Three criteria were employed in judging the "success" of a trip: (1) development of higher suction pressures, (2) further delay of stall, and (3) elimination of the separation bubble, when compared with the flow over the untripped airfoil. Results for the best trip (trip #4) are summarized here. Results for all the trips were reported by Wilder et al [11], and Chandrasekhara et al [22].

It was shown in Ref. 22 that steady stall changed from an abrupt leading-edge stall to a more gradual stall resembling trailing-edge stall. Such a radical change in the character of the stall highlights the sensitivity of the flow to the trip type. The development of the leading edge suction pressure for unsteady flow is plotted in Fig. 14 for untripped and tripped airfoils oscillating with a reduced frequency of k = 0.05. The free stream Mach number for the experiments was M = 0.3 for Fig. 14a and M = 0.45 for Fig. 14b. For both Mach number flows, the peak suction pressure is greatest on the tripped airfoil (criterion 1), and for the M = 0.3 case, stall was delayed by approximately one degree. Surface pressure distributions are shown for M = 0.3; k = 0.05; $\alpha = 10.65^0$, and M = 0.45; k = 0.05; $\alpha = 7.97^0$ in Figs. 15a and 15b, respectively. In both cases a higher pressure was developed and the separation bubble was eliminated. The greatest increases in suction pressure occur in the high Mach number case which implies that the viscous/inviscid interactions are strongly influenced by the presence of the laminar separation bubble.

An examination of the global flow fields of the untripped and tripped flows will further illustrate the effects of tripping. Pressure coefficient fields determined from PDI images are shown in Fig. 16 for M = 0.3; k = 0.05; $\alpha = 13.99^0$ for untripped and tripped airfoils. In Fig. 16a the flow is separated at the leading edge of the airfoil, and the dynamic stall vortex has convected just beyond the quarter chord point. The airfoil has lost its suction peak: $C_{p_{min}} = -3.89$ compared with -5.50 for the tripped airfoil. The dynamic stall vortex is still in the earliest stage of development in the flow over the tripped airfoil (see Fig. 16b).

Global pressure coefficient fields for M = 0.45; k = 0.05; and $\alpha = 10.0^0$ are shown in Fig. 17. The data in Fig. 17a (repeated from Fig. 10 for convenience) is for the untripped airfoil, while Fig. 17b is for the tripped airfoil. The tripped airfoil developed higher suction pressures, but the onset of dynamic stall was advanced slightly. More significantly, the shock structure and the number of compressions/expansions was dramatically altered in comparison with the untripped flow. This again points to a strong influence of the separation bubble on the viscous/inviscid interactions in the flow.

C. Image Analysis

Massive amounts of data can be obtained using the interferometry and imaging techniques described previously and, when properly analyzed, each image can yield detailed, quantitative information on both the surface- and global-pressure distributions of the flow. The analysis procedure begins with rendering the photographic images in digital form for representation and manipulation on a computer work station. Digitization is performed with a Sharp color scanner at 300 dpi (dots per inch) resolution. Grayscale images are created with 256 possible intensity levels for each pixel. Images are typically from 700 to 900 square pixels in size requiring approximately 0.5 to 1 Megabyte of storage on the computer. To help eliminate any possible operator bias from the analysis of the images, an automatic fringe analysis technique was developed. The analysis of interferometric fringe patterns is well suited to computer automation. In theory, an interference pattern is a simple sinusoidal variation in intensity between light to dark shades of grey. Fringes could be identified by locating intensity maxima within the image. In practice though, there are noise signals, spurious signals, and extreme variation in contrast (or fringe visibility) added to the fringe patterns, all of which complicate the analysis procedures.

The noise inherent in each image is the principal obstruction to automating the analysis process. The noise sources present in the PDI system can be classified as producing either spurious fringes, or a random background signal. The first class includes fringes produced by diffraction off the edges of the airfoil model and off imperfections in the system optics. Also included in this class is optical distortion [23] produced by the large density gradients encountered in regions of the flow. These distortions manifest as under- and over-exposed areas near the leading edge of the airfoil and may cause breaks to appear in the fringes. Spurious fringes can be removed form the final analysis only by human intervention or by giving the program some level of intelligence. Currently, human intervention is required.

The second class of noise is a random signal produced by a combination of laser speckle and film/scanner resolution. Laser speckle cannot be avoided in the absence of perfect optics, but can be minimized by keeping the optics as clean as possible. The Type-57 Polaroid film used has a resolution of 18-22 line pairs/mm (457-559 /inch), while the scanner resolution is 12 dots per mm (300 dpi) at 8 bits per dot. Examples of this random noise is represented in Fig. 18, which shows the intensity variation along a row of pixels taken from two "blank" images. A blank is an image of the laser beam with the point-diffraction source removed from the system, and the wind tunnel flow turned off. The top line in Fig. 18 is from an over-exposed image and the bottom line is from an under-exposed image. The mean intensity of each line is approximately that of the peak of a light and dark fringe, respectively. This random component, therefore, is independent of the exposure, and since on interference occurs for a "blank" image, the noise must be independent of fringe visibility. Consequently, both high- and low-contrast images contain the same random noise component.

A typical PDI image was chosen as a test image and is shown in Fig. 19. The flow conditions for this image were: $M = 0.3$; $k = 0.05$; $\alpha = 10^0$; $Re = 0.6x10^6$; and untripped. The image is of moderate contrast with below average contrast in most of the lower half of the image. There is also a set of concentric diffraction rings, caused by a damaged region on the transmitting Schlieren mirror, centered on the bottom edge of the image. The three black triangular shapes are coordinate registration marks located on the glass window of the test section. It is interesting to note that, while the low contrast fringes are easily detected by a human observer, the diffuse edges and shallow intensity gradients make machine detection quite difficult. The width of the fringes varies dramatically across the image, from several hundred pixels in the outer flow to only a few pixels near the leading edge, where the resolution limit of the film can be reached. Consequently, the information content of each image is spread over a wide range of frequencies and so filtering of the image (whether in the frequency or the spatial domain) must be adaptable to the local image characteristics.

1. Digital Filtering

Two rows of pixels are highlighted in Fig. 19. These rows will be used to illustrate the effects of several filters. The intensity profile along the upper, full row of pixels is plotted as a dotted line in Figs. 20a-20c. The pixel intensity ranges from 0 (black) to 255 (white). In the case of Fig. 20c the range has been scaled to -1.0 to 1.0 for computational purposes. The intensity profile for the second, short row is plotted in Figs. 21a-21c. The results from two spatial low-pass filter methods are plotted in Figs. 20a/b and 21a/b. The first filter studied (Figs. 20a and 21a) is a simple moving window average of seven pixels. That is, each pixel is replaced with the average of its seven nearest neighbors. This filter efficiently removed the noise from the wide fringes (Fig. 20a) while preserving the signal, but obliterated the narrow fringes (Fig. 21a). This is because the narrow fringes have a frequency very nearly that of the system noise. In fact, the particular narrow fringe signal illustrated in Fig. 21 does not require any filtering. In practice this portion of the image must be treated separately.

A directional version of the moving window average, called a spin-filter [24], was studied which improves the filters performance near closely spaced fringes. The spin-filter aligns a one-dimensional averaging window to the direction of minimum local intensity gradient. This way blurring of fringe edges is reduced. In regions of wide fringes, however, the local intensity gradients are often dominated by the noise. Consequently, the alignment of the spin-filter becomes random and portions of the noise signal are preserved (see Fig. 20b). Results for a seven pixel spin-filter are presented in Figs. 20b and 21b for wide and narrow fringes, respectively.

Better smoothing can be achieved by fitting an approximating polynomial to the noisy data [25]. The results of approximation using Chebyshev polynomials are illustrated in Figs. 20c and 21c for wide and narrow fringes, respectively. The data were divided into sub-units, using a threshold edge detection algorithm. A Chebyshev approximating polynomial of order 20 was fit to the data on each sub-unit, then evaluated using only the first 7 coefficients. The data were divided into sub-units to reduce the number of coefficients required to produce a smooth fit.

2. Fringe Centerline Extraction

Intensity gradients are calculated at each pixel of the filtered image using the following finite difference formulations:

$$\frac{\partial g_{i,j}}{\partial x} = \frac{-3g_{i,j} + 4g_{i+1,j} - g_{i+2,j}}{2},$$

$$\frac{\partial g_{i,j}}{\partial x} = \frac{3g_{i,j} - 4g_{i-1,j} + g_{i-2,j}}{2},$$

$$\frac{\partial g_{i,j}}{\partial x} = \frac{-g_{i+2,j} + 8g_{i+1,j} - 8g_{i-1,j} + g_{i-2,j}}{12}.$$

Both the x- and y-derivatives are evaluated at each pixel. A new direction field is calculated to indicate if the local fringe direction is more nearly horizontal or vertical - a fringe running at ±45 deg. is arbitrarily labeled "more nearly horizontal".

Fringe centerlines are located by finding zero-crossings (or slope changes) in the intensity gradients. The x-component ($\frac{\partial g_{i,j}}{\partial x}$) of the gradient is examined if the direction at the current pixel was found to be vertical, and, conversely, $\frac{\partial g_{i,j}}{\partial y}$ is examined if the direction was found to be horizontal. A threshold is used to avoid false detections due to noise in the derivatives. A zero-cross is considered valid only if the magnitude of the gradient exceeds this threshold before the next zero-crossing occurs. The centerline pixels are coded to indicate membership with a light or dark fringe.

The images shown in Fig. 22b and 22c illustrate the results of applying some of the digital filters described previously to a full image. The image in Fig. 22a was recorded for the following conditions: M = 0.3; k = 0.05; and $\alpha = 10^{0}$. The enhanced image obtained by global histogram equalization [26] is shown in Fig. 22b. The enhanced imaged was then smoothed by five iterative applications of the spin filter using a 7 x 7 pixel mask (see Fig. 22c). The fringe centerlines extracted from these images are shown in Fig. 23a and 23b, respectively. For clarity, only the dark fringes are shown, and the data are plotted in the model fixed coordinate system. These two examples show how smoothing (low-pass filtering) improves the ability of the algorithm to trace the wide fringes, yet smooths away the small scale detail near the leading edge.

A second example is given in Figs. 24 and 25 to illustrate the use of enhancement with local histogram equalization. The flow conditions for the image shown in Fig. 24a were M = 0.45; k = 0.05; and $\alpha = 10^{0}$. A magnified view of the upper surface of the leading edge of the airfoil is shown, and multiple compression shocks can be seen. Two low contrast regions, one under exposed and the other over exposed, are highlighted on the figure. Global histogram equalization does little to enhance these regions (see Fig. 24b), and gaps exist in the extracted fringes (see Fig. 25a). Histogram equalization using *local* parameters on each 15 x 15 pixel sub-region of the image greatly enhance the details in the low contrast regions of the image, as is shown in Fig. 24c. However, this technique also enhances background noise, and is of use only where the fringes are narrow. The fringe centerlines extracted from this image are shown in Fig. 25b.

IV. Conclusions

The results of the cooperative agreement no. NCC2-637 have been highlighted in this final report. A parametric study of compressible dynamic stall of airfoils was performed. This study has added greatly to the understanding of how the unsteady separated flow associated with dynamic stall can be controlled. The study was conducted experimentally using point diffraction interferometry (PDI), a nonintrusive technique which yields instantaneous full-field visualizations of the fluid density. When coupled with digital image analysis techniques, quantified pressure fields can be extracted from the visualization images. Flow parameters varied included Mach number, pitch rate, pitch history, Reynolds number, and leading-edge surface roughness of the airfoil. The angle of attack at which the flow separates decreases with increasing free stream Mach number. The effects of flow compressibility exist at the relatively low free stream Mach number of 0.3. Consequently, the control of dynamic stall will require the suppression of the effects of compressibility.

An airfoil with a dynamically adaptive leading-edge profile was proposed as a device for the actively suppressing the compressibility effects. The technique involves varying the nose shape to a supercritical profile as compressibility becomes critical. A model was installed in the Compressible Dynamic Stall Facility and will be tested soon.

The onset of the dynamic stall process begins with a rapid coalescence of vorticity leading to the formation of the dynamic stall vortex. This process occurs over less that one half of a degree of motion of the pitching airfoil. Furthermore, the process is highly nonlinear and does not repeat exactly form event to event. To capture this detail in real time a high-speed phase-locked photographic data acquisition system was developed for recording interferometry images at rates up to 40,000 images/sec. The system will also be used to document the instantaneous shape of the deforming surface of the adaptive-geometry airfoil.

A semi-automatic computer-aided algorithm was developed for mapping the centerlines of interferometric fringe patterns. Automatic processing eliminates operator bias as a potential source of error in tracing the fringes, and significantly reduces the effort required to process an image. Manual processing requires the user to painstakingly trace each fringe; a tedious procedure which leaves the user fatigued after processing a few images. Processing times on the Personal IRIS 4D range from 1 to 15 minutes depending on the size of the image and the number of filter and enhancement steps performed. The algorithm represents a substantial time savings over the manual processing time of 30-60 minutes per image.

V. References

[1] Chandrasekhara, M.S. and Carr, L.W., "Flow Visualization Studies of the Mach Number Effects on the Dynamic Stall of an Oscillating Airfoil", *Journal of Aircraft*, Vol. 27, No. 6, pp. 516-522.

[2] Carr, L.W., McCroskey, W.J., McAlister, K.W., Pucci, S.L., and Lambert, O., "An Experimental Study of Dynamic Stall on Advanced Airfoil Sections Volume 3. Hot-Wire and Hot-Film Measurements", *NASA-TM-84245*, Dec. 1982.

[3] Ahmed, S., "Control of Unsteady Separated Flow Associated With the Dynamic Stall of Pitching Airfoils", *MCAT Institute Progress Report*, December, 1991.

[4] Wu, J. Z., Vakili, A. D., and Wu, J. M., "Review of the Physics of Enhancing Vortex Lift by Unsteady Excitation", *Prog. Aerospace Sci.*, Vol. 28, 1991, pp. 73-131.

[5] Rossi, M. J., Austin, F., and VanNostrand, W., "Active Rib Experiment for Shape Control of an Adaptive Wing", *AIAA Paper 93-1700*, 1993.

[6] Tsukamoto, H., Tanaka, K., Matsunaga, S., and Tanaka, H., "Development of a Shape-Controlled Airfoil by Use of SMA", *Japan Society of Mechanical Engineers, Transactions B*, Aug. 1992, pp. 169-173.

[7] Carr, L.W., and Chandrasekhara, M.S., "Design and Development of a Compressible Dynamic Stall Facility", *Journal of Aircraft*, Vol. 29, No. 3, pp. 314-318.

[8] Chandrasekhara M.S., and Carr, L.W., "Design and Development of a Facility for Compressible Dynamic Stall Studies of a Rapidly Pitching Airfoil", *ICIASF'89 RECORD*, IEEE Publication 89-CH2762-3, pp. 29-37.

[9] Nakamura, Y., and Tomonari, Y., "The Effects of Roughness on the Flow Past Circular Cylinders at High Reynolds Numbers", *Journal of Fluid Mechanics*, Vol. 123, 1982, pp. 363-378.

[10] Pope, A., and Goin, K.L., *High Speed Wind Tunnel Testing*, Kraeger Publishing Company, New York, NY, 1978.

[11] Wilder, M.C., Chandrasekhara, M.S., and Carr, L.W., "Transition Effects on Compressible Dynamic Stall of Transiently Pitching Airfoils", AIAA Paper 93-2978, July, 1993.

[12] Carr, L.W., Chandrasekhara, M.S., Ahmed, S., and Brock, N.J., "A Study of Dynamic Stall Using Real Time Interferometry", *AIAA Paper 91-0007.*

[13] Brock, N.J., Chandrasekhara, M.S., and Carr, L.W., "A Real Time Interferometry System for Unsteady Flow Measurements", *The 14th ICIASF Conference*, Rockville, MD, Oct. 1991.

[14] Goldstein, R.J., "Optical Systems for Flow Measurement: Shadowgraph, Schlieren, and Interferometric Techniques", *Fluid Mechanics Measurements*, Hemisphere, New York, 1985, pp.377-422.

[15] Wilder, M. C., "Control of Unsteady Separated Flow Associated With the Dynamic Stall of Airfoils", *NASA-CR-190688*, August, 1992.

[16] Chandrasekhara, M. S., Squires, D. D., Wilder, M. C., and Carr, L. W., "A Phase-Locked High-Speed Real-Time Interferometry System for Large Amplitude Unsteady Flows", 7th International Symposium on Applications of Laser Techniques to Fluid Mechanics, Lisbon, Portugal, July, 1994.

[17] Beard, J., "Plastic Ribbon Shakes the Ice off Aircraft", *New Scientist*, May 12. 1990, p. 36.

[18] Wilder, M. C., "Control of Unsteady Separated Flow Associated With the Dynamic Stall of Airfoils", *MCAT Institute Annual Report 94-20*, July, 1994.

[19] Chandrasekhara, M.S., Ahmed, S., and Carr, L.W., "Schlieren Studies of Compressibility Effects on Dynamic Stall of Transiently Pitching Airfoils", *Journal of Aircraft*, Vol. 30, No. 2, March-April 1993, pp. 213-220.

[20] Chandrasekhara, M.S., Carr, L.W., and Wilder, M.C., "Interferometric Investigations of Compressible Dynamic Stall Over a Transiently Pitching Airfoil", *AIAA Journal*, Vol. 32, No. 3, 1994, pp. 586-593.

[21] Ackeret, J., Feldmann, F., and Rott, N., "Investigations of Compression Shocks and Boundary Layers in Gases Moving at High Speed", *NACA TM-1113*, 1947.

[22] Chandrasekhara, M.S., Wilder, M.C. and Carr, L.W., "Boundary Layer Tripping Studies of Compressible Dynamic Stall Flow", *AIAA-94-2340*, 25th AIAA Fluid Dynamics Conference, Colorado Springs, CO, June 20-23, 1994.

[23] Cho, Y.C., Carr, L.W., and Chandrasekhara, M.S., "Corrections to Fringe Distortion due to Flow Density Gradients in Optical Interferometry", AIAA-93-0631, 31st Aerospace Sciences Meeting, Reno, NV, Jan. 11-14, 1993.

[24] Yu, Q., "Spin Filtering Processes and Automatic Extraction of Fringe Centerlines in Digital Interferometric Patterns", *Applied Optics*, Vol. 27, No. 18, 15 Sep. 1988, pp. 3782-3784.

[25] Press, H.P., Teulolsky, S.A., Vetterling, W.T., and Flannery, B.P., *Numerical Recipes in C*, Cambridge University Press, 1992, pp. 190-196.

[26] Gonzalez, R.C., and Woods, R.E., *Digital Image Processing*, Addison-Wesley Publishing Company, Inc., 1992, pp. 173-185.

Table 1: PDI Data for Pitching 7.62cm Chord NACA 0012

M	α^+					
	0	0.02	0.025	0.03	0.035	0.04
0.20	1,2,3		1,2,3	1,2,3	2,3	1,2
0.25	2		2,3	2,3	2	2
0.30	1,2,3	1,2,3	1,2,3	1,2,3	1,2,3	1,2,3
0.35	2,3	2,3	2,3	2,3	2	2
0.40	2,3	2,3	2,3	2,3	2	
0.45	1,2,3	1,2,3	1,2,3	1,2,3		

1 Trip #1, Leading Edge Flow Studies
2 Untripped Leading Edge Flow Studies
3 Untripped Global Flow Studies

Table 2: PDI Data for Oscillating 7.62cm Chord NACA 0012

M	k					
	0	0.025	0.05	0.075	0.1	0.15
0.20	2,3 7		1,2,3 6,7	1 6,7	1,2,3 7	7 7
0.25			6	6	6	
0.30	2,3,4 5,6,7	1 6,7	1,2,3,4 5,6,7	1 6,7	1,2,3,4 6,7	
0.35		6	6	6		
0.40	7	6,7	6,7	6,7	7	
0.45	2,3,4 5,7	1 6,7	1,2,3,4 5,6,7	6,7 6,7		

1	Trip #1, Leading Edge Flow Studies
2	Trip #2, Leading Edge Flow Studies
3	Trip #3, Leading Edge Flow Studies
4	Trip #4, Leading Edge Flow Studies
5	Trip #5, Leading Edge Flow Studies
6	Untripped Leading Edge Flow Studies
7	Untripped Global Flow Studies

Table 3: PDI and Pressure Data for Oscillating 15.24cm Chord NACA 0012

M	k		
	0	0.05	0.1
0.20	1, P1	1	1
0.30	1, P1	1	1
	2, P2	2	2
0.35	1, P1	1	
	2, P2	2	
0.40	1, P1	1	
	2, P2	2	
0.45	1, P1	1	
	2, P2	2	

1	Untripped Leading Edge PDI Flow Studies
P1	Untripped Steady Surface Pressures
2	Tripped Leading Edge PDI Flow Studies
P2	Tripped Steady Surface Pressures

(a)

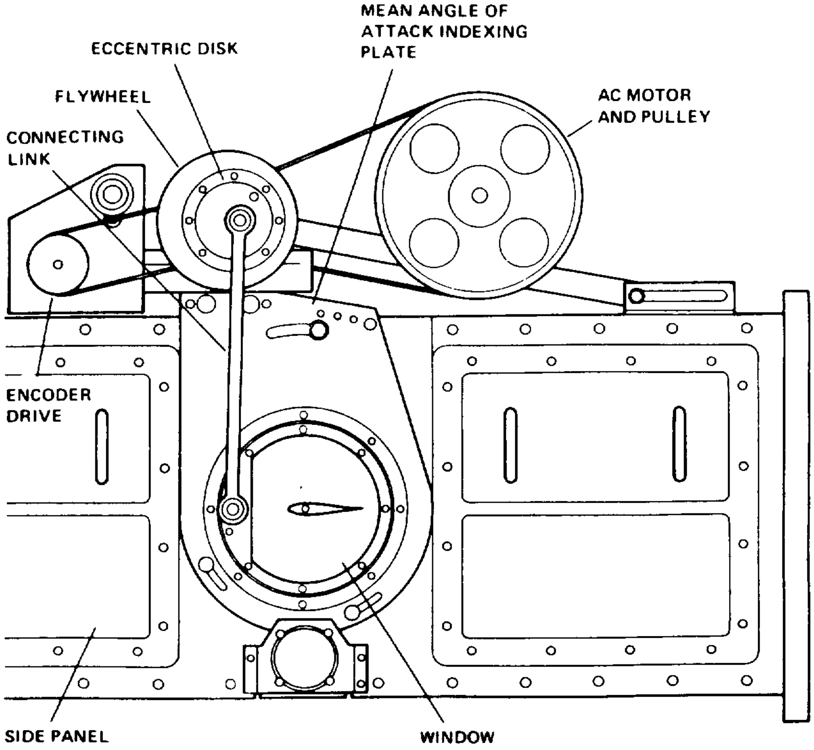

(b)

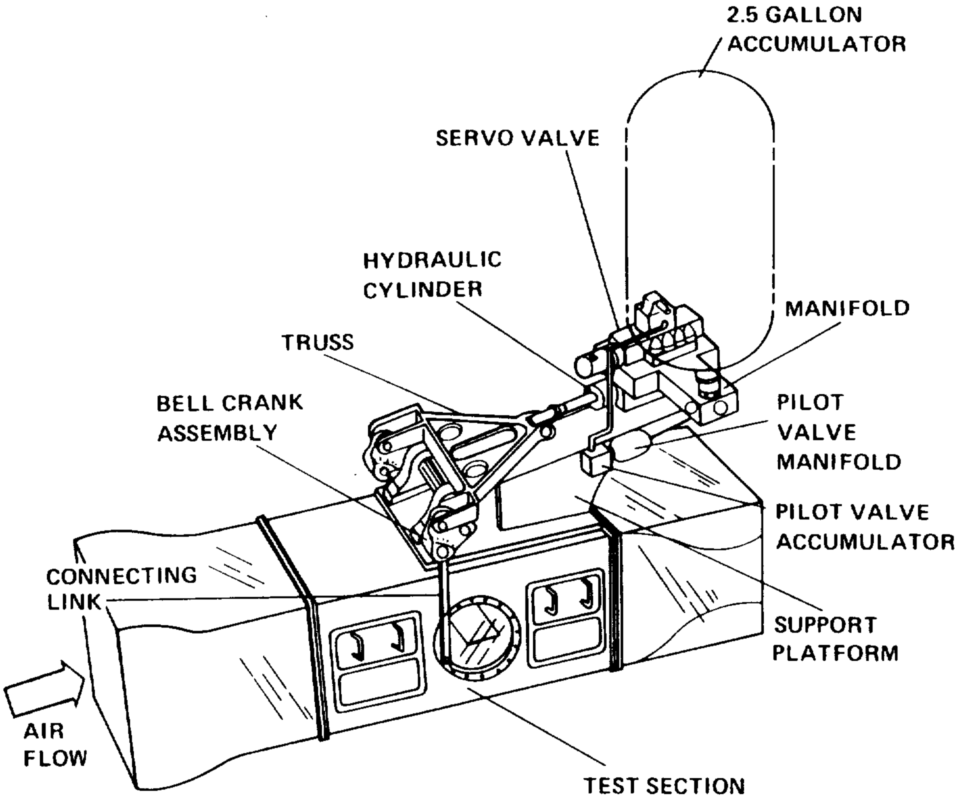

Fig. 1. Diagrams of the Compressible Dynamic Stall Facility: (a) with AC Motor for Sinusoidal Oscillations; (b) with Hydraulic Drive for Transient Pitch Motions.

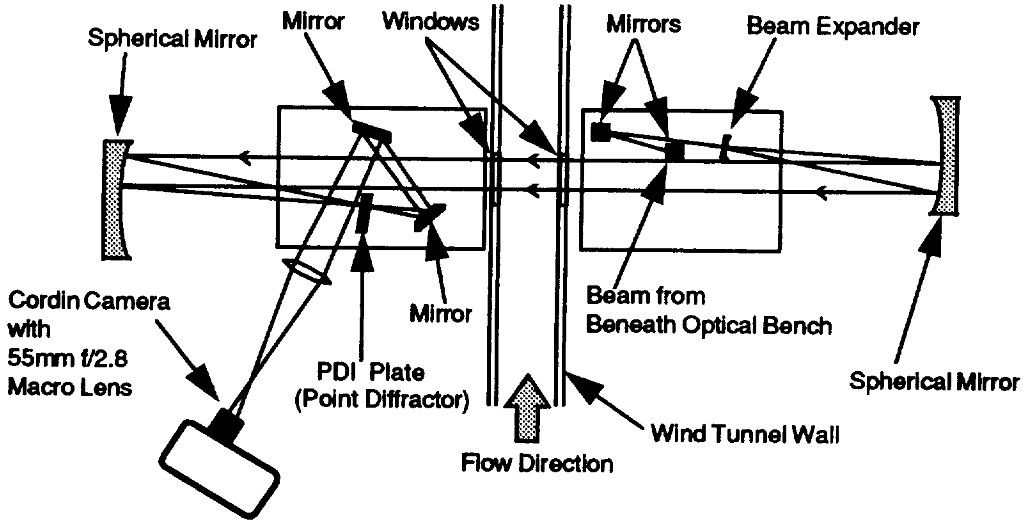

Fig. 2. Optical Arrangement of the PDI System.

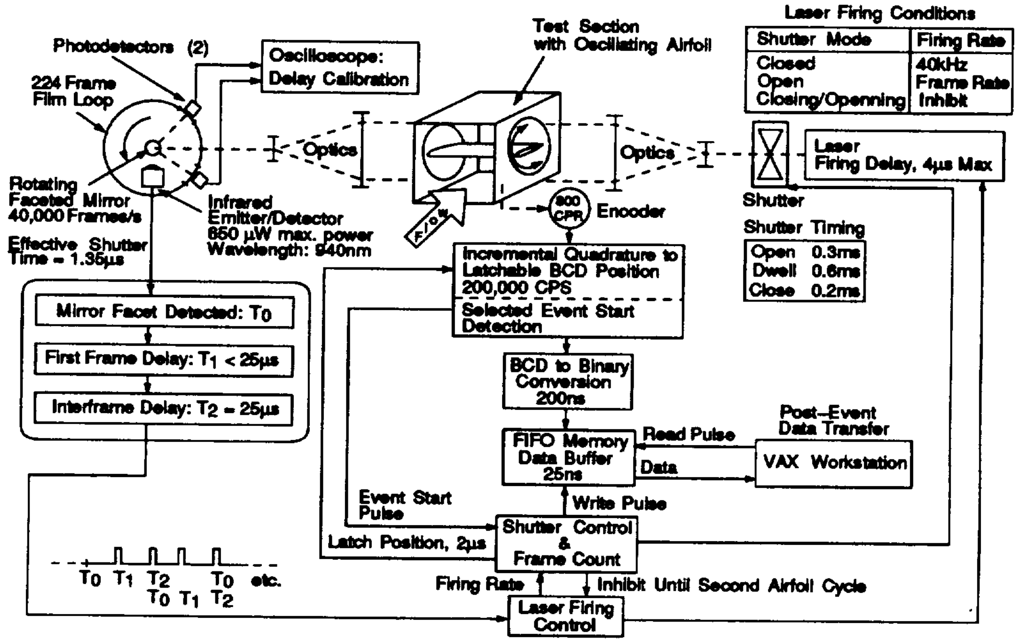

Fig. 3. Block Diagram of Camera/Laser Synchronization for the High–Speed Interferometry System.

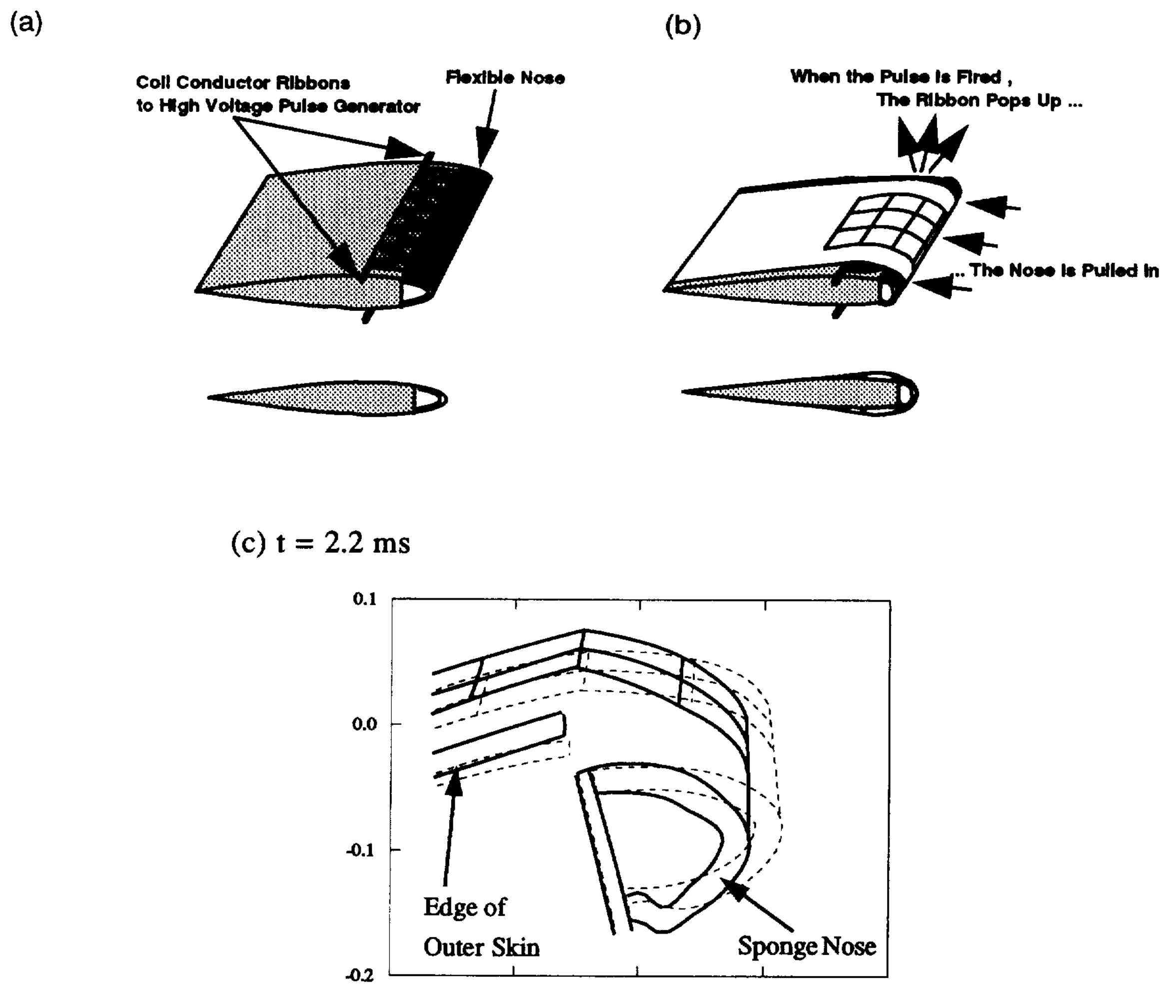

Fig. 4. Sketch of Electro-repulsive Dynamically Deformable Leading Edge Device: (a) Neutral Profile (NACA 0012), (b) Deformed Profile (Outer Skin and Measurement Grid Shown), (c) Measured Profile 2.2ms After Pulse.

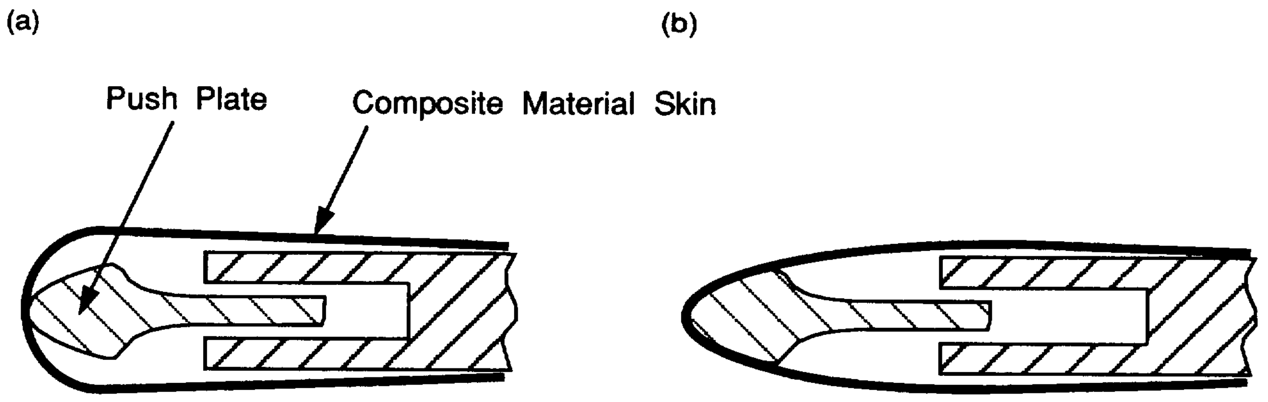

Fig. 5. Sketch of Dynamically Deformable Leading Edge Device: (a) Push Plate Retracted; Outer Skin Has Circular Profile, (b) Push Plate Extended; Outer Skin Has Sharp (NACA 0012) Profile.

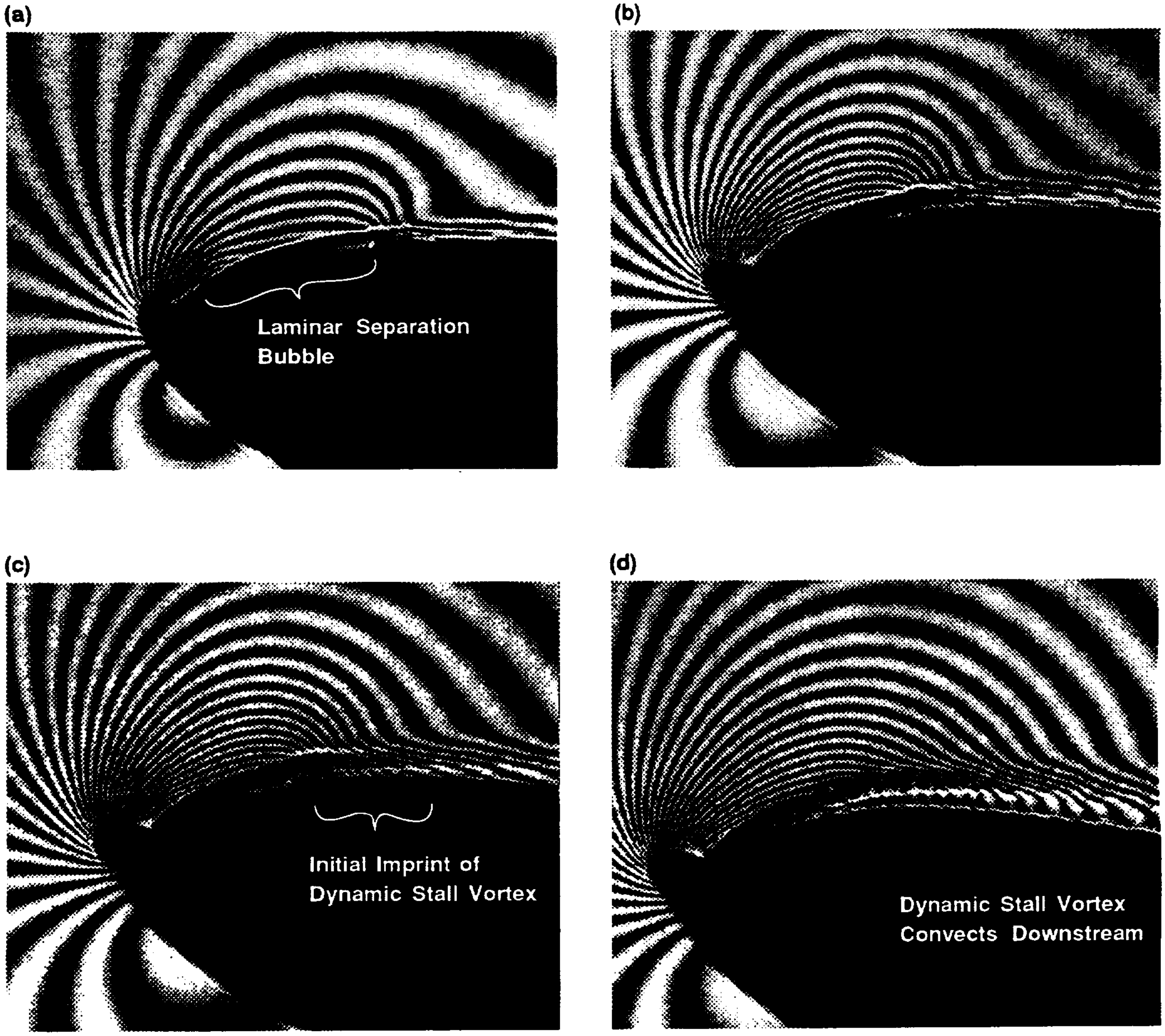

Fig. 6. Sequence of PDI Images Depicting the Bursting of the Laminar Separation Bubble and the Inception of the Dynamic Stall Vortex for Flow over an Oscillating Airfoil with $M = 0.3$; $k = 0.1$: (a) $\alpha = 10.0°$; (b) $\alpha = 12.0°$; (c) $\alpha = 13.0°$; (d) $\alpha = 14.0°$.

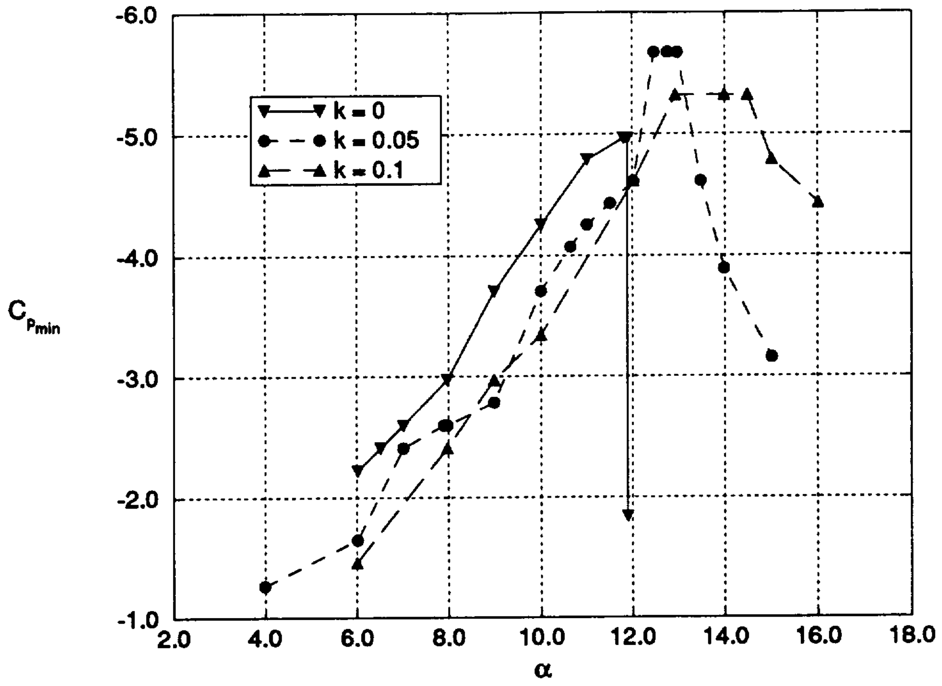

Fig. 7. Effect of Forced Unsteadiness on Airfoil Peak Suction Development: M = 0.3.

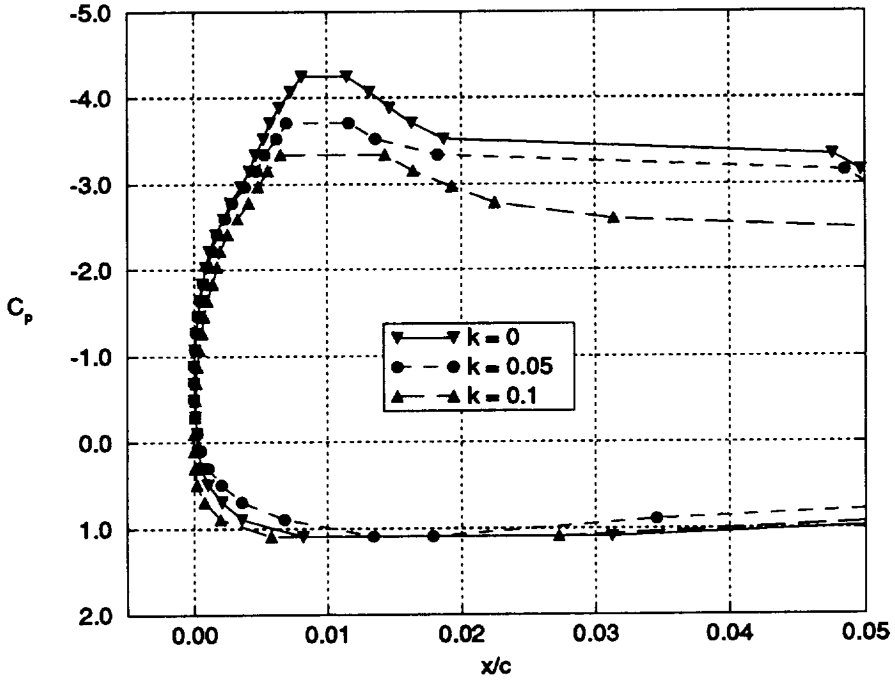

Fig. 8. Effect of Forced Unsteadiness on Airfoil Leading-Edge Pressure Distribution: M = 0.3; α = 10°.

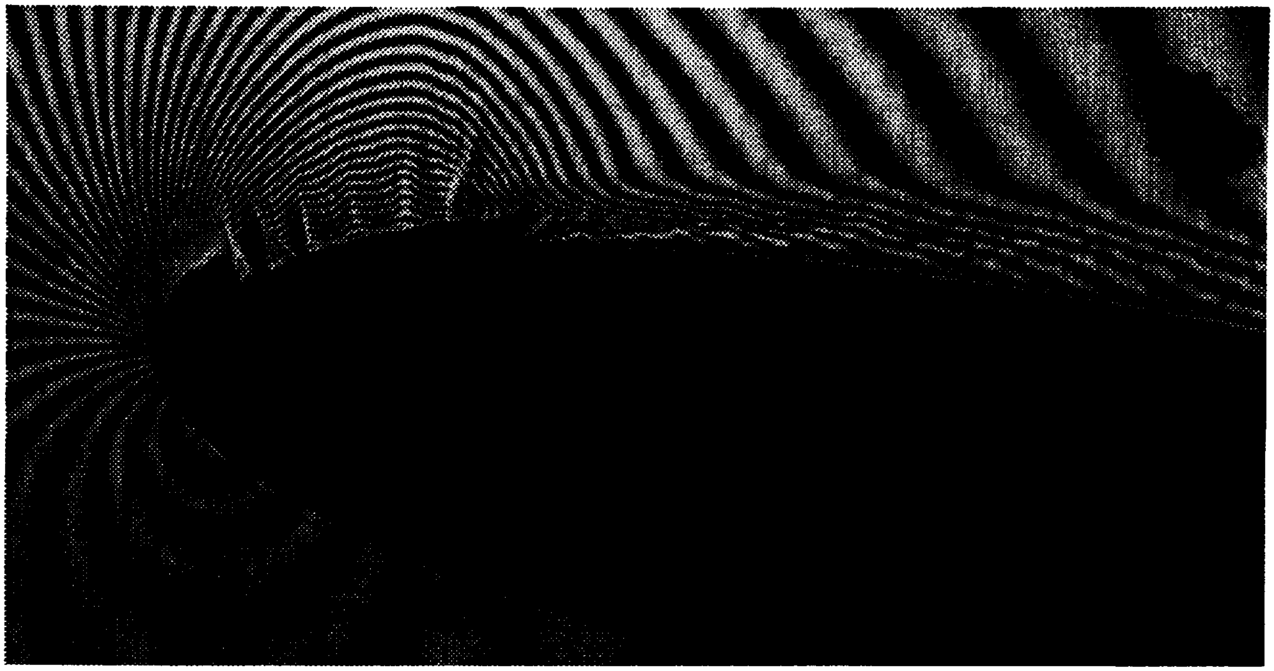

Fig. 9. PDI Image Showing Multiple Shocks over Untripped Oscillating Airfoil: M = 0.45; k = 0.05; α = 10°.

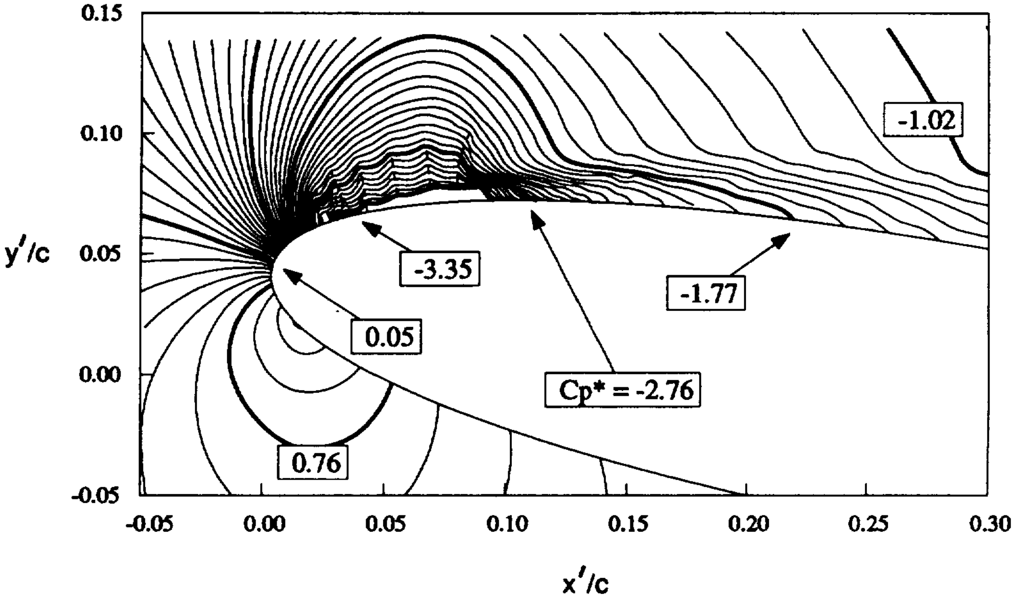

Fig. 10. Global Pressure Field Determined from Analysis of Image Shown in Fig. 6: M = 0.45; k = 0.05; α = 10°.

Fig. 11. Effect of Compressibility on Dynamic Stall Flow over Oscillating Airfoil: $\alpha = 12^{o}$; $k = 0.05$. (a–d): PDI images; (e–h): Color coded pressure coefficient fields extracted from the images. Red indicates critical pressure coefficient, C_p^*.

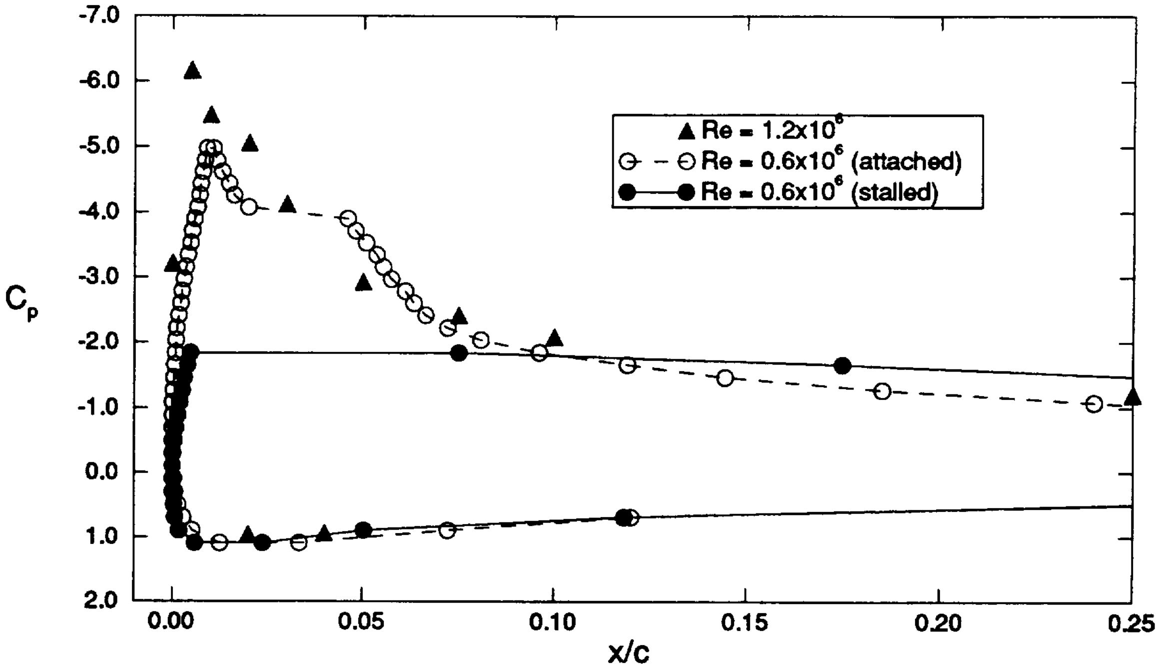

Fig. 12. Effect of Reynolds Number on Surface Pressure Coefficient Distribution: M = 0.3; k = 0; α = 12°.

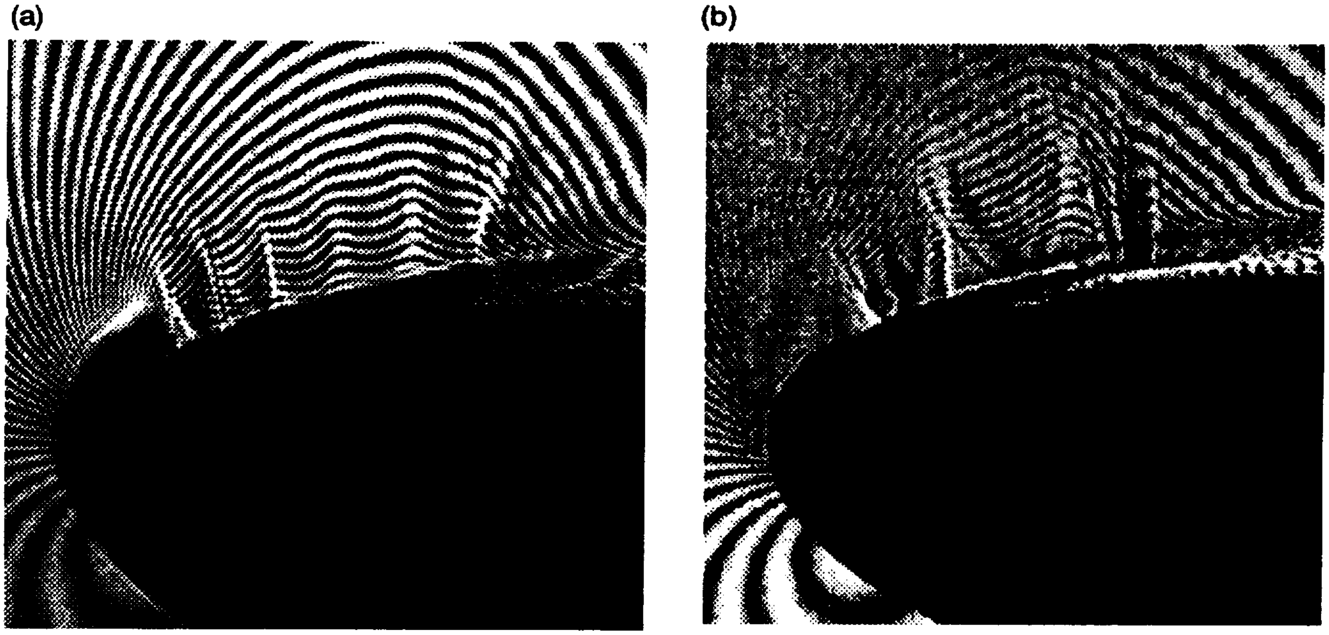

Fig. 13. Effect of Reynolds Number on Shock Structure for Oscillating Airfoil: M = 0.45; k = 0.05; α = 10°. (a) Re = 0.81x10^6 (7.62cm Chord Airfoil), (b) Re = 1.62x10^6 (15.24cm Chord Airfoil).

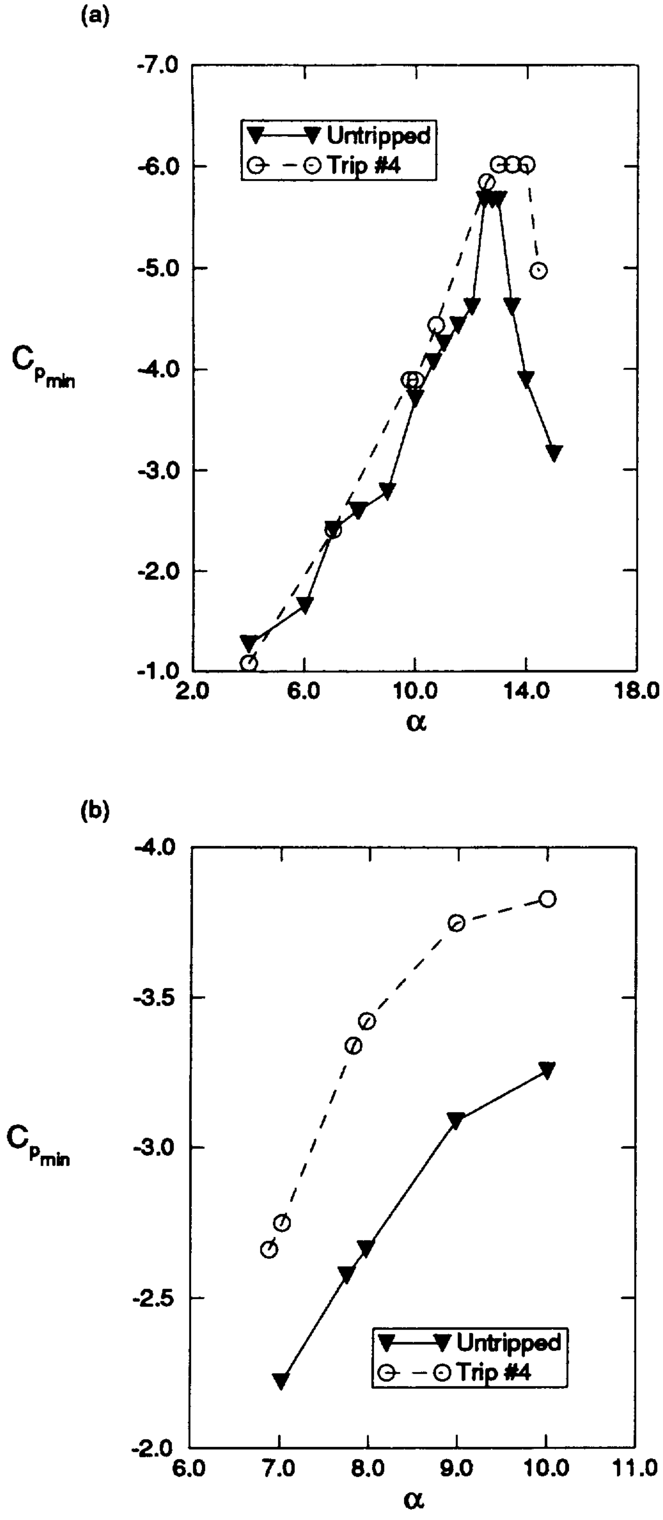

Fig. 14. Effect of Tripping on Development of Peak Suction Pressure Coefficient for k = 0.05: (a) M = 0.3, (b) M = 0.45.

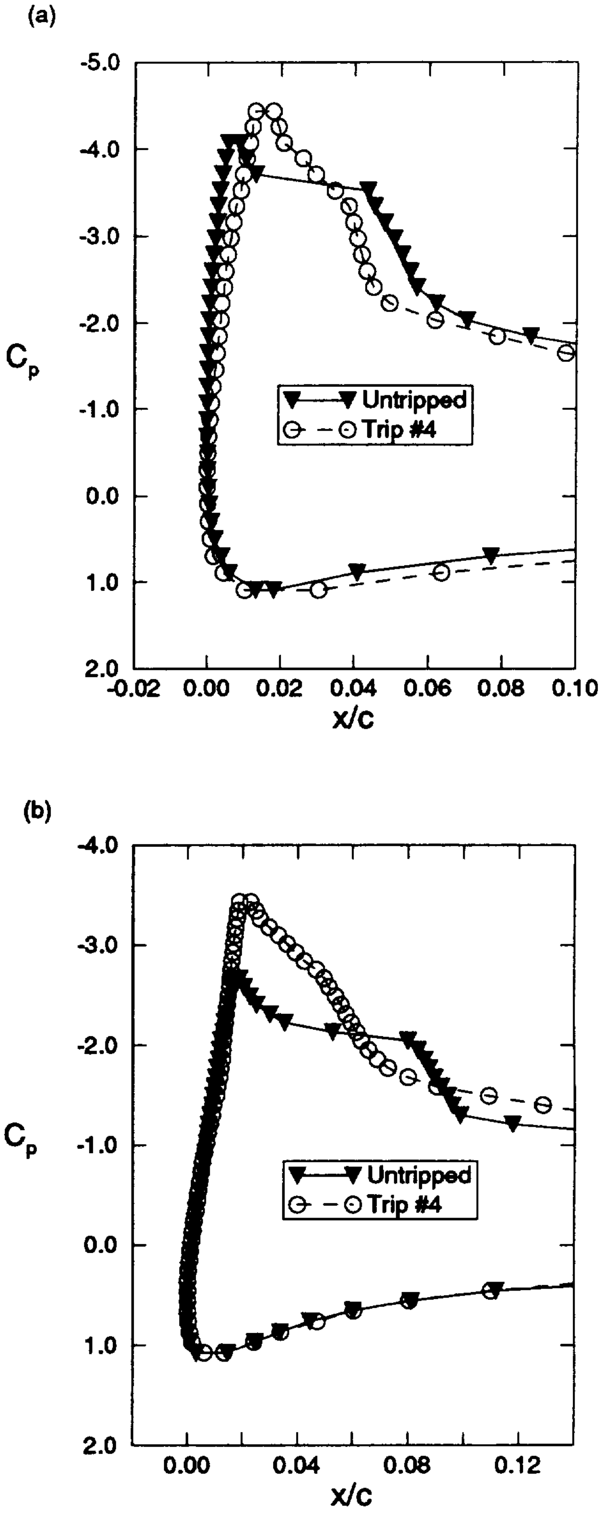

Fig. 15. Effect of Tripping on Surface Pressure Coefficient Distribution for k = 0.05: (a) M = 0.3, α = 10.65°, (b) M = 0.45, α = 7.97°.

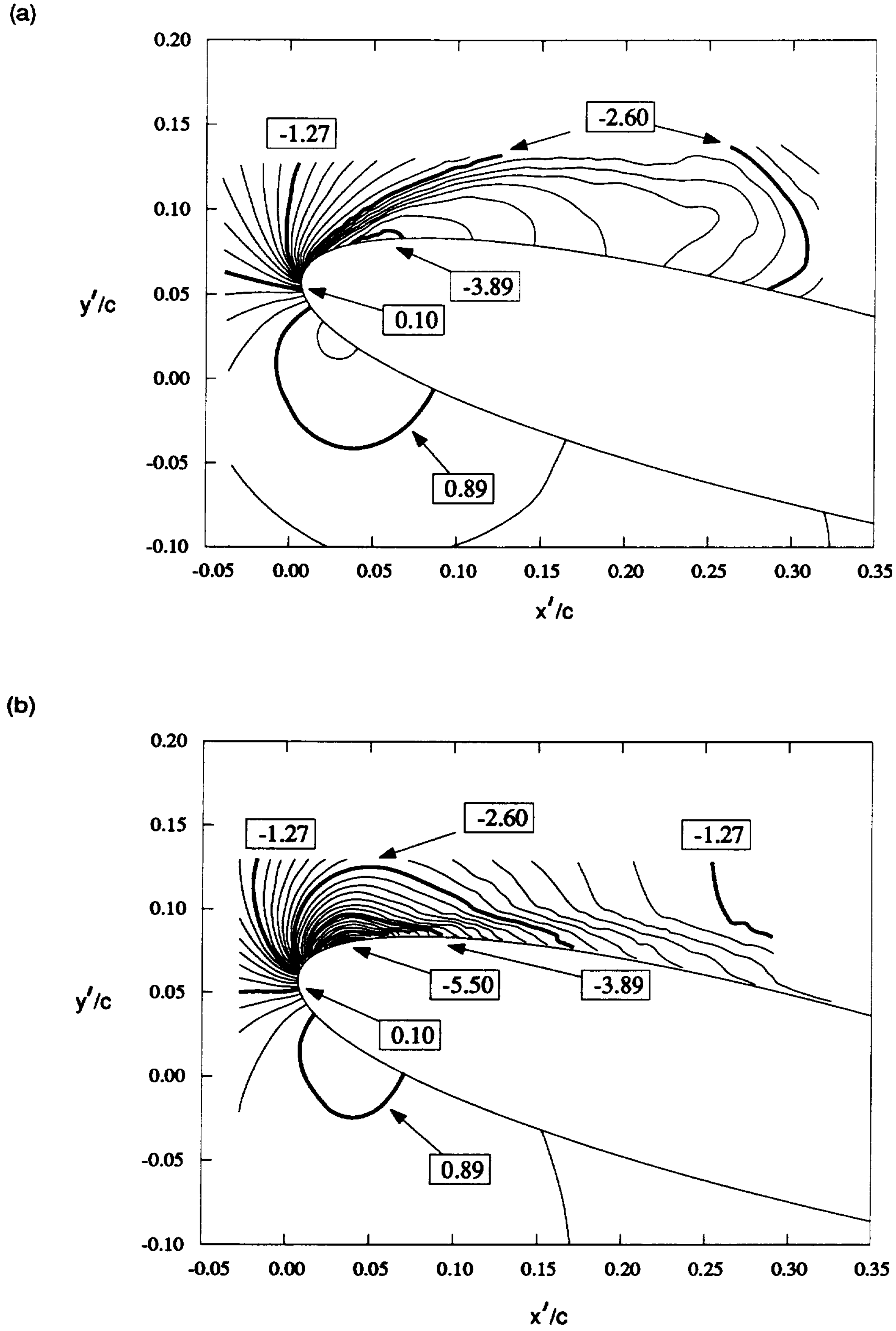

Fig. 16. Global Pressure Coefficient Fields for Flow at M = 0.3; k = 0.05; $\alpha = 13.99^{o}$: (a) Untripped Airfoil, (b) Tripped Airfoil, Trip #4.

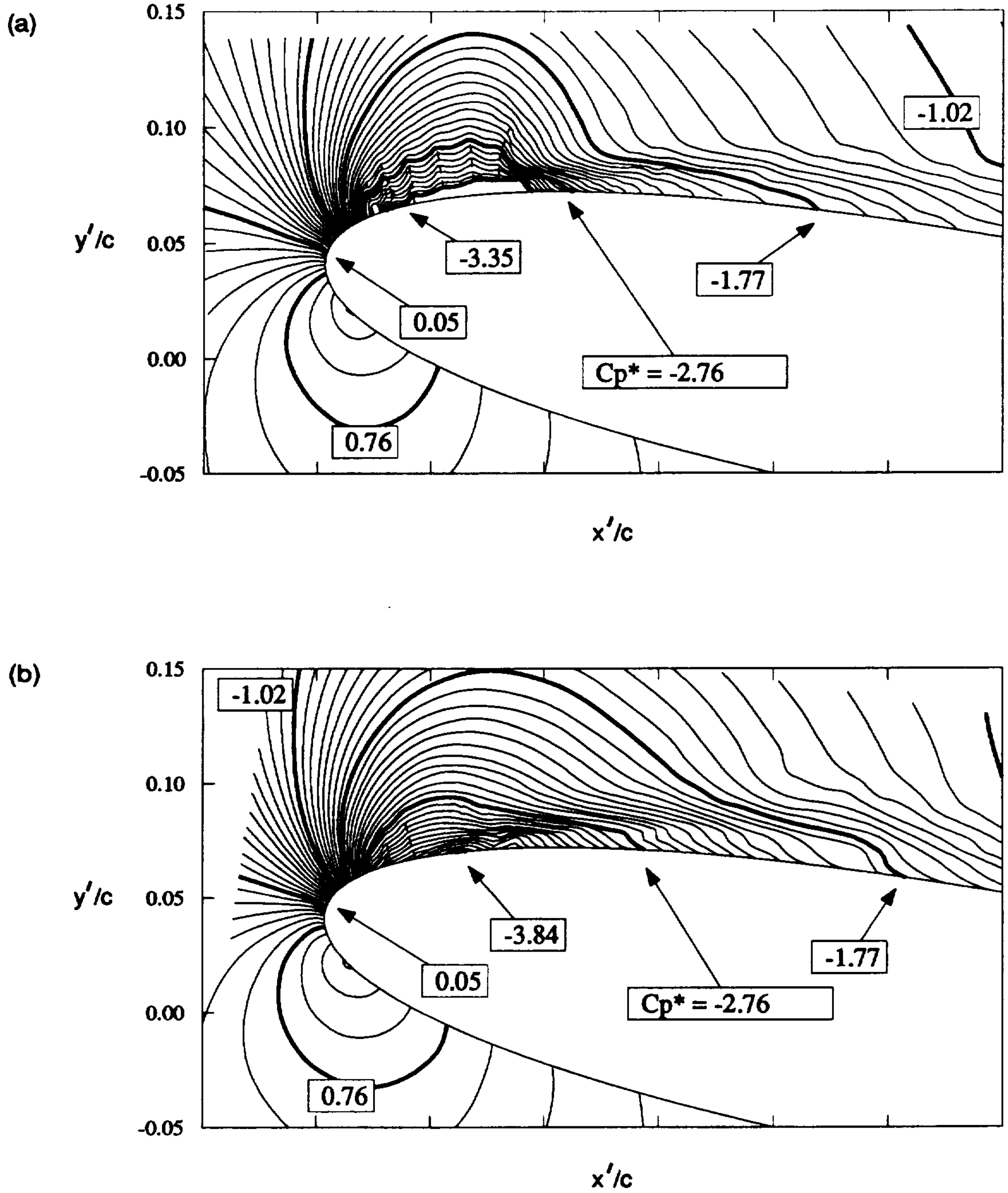

Fig. 17. Global Pressure Coefficient Fields for Flow at M = 0.45; k = 0.05; $\alpha = 10.0^{\circ}$: (a) Untripped Airfoil, (b) Tripped Airfoil, Trip #4.

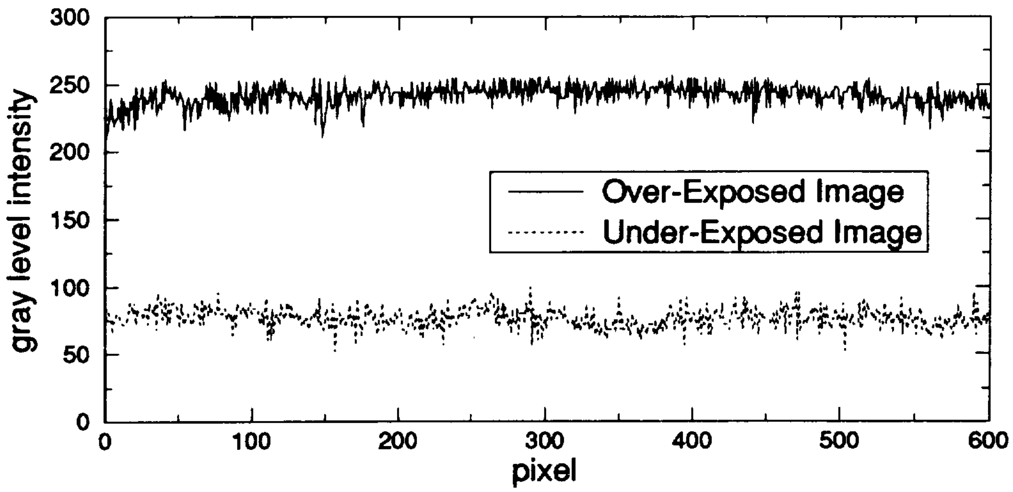

Fig. 18. Background Noise Component of PDI Images Taken From Images of the Laser Beam.

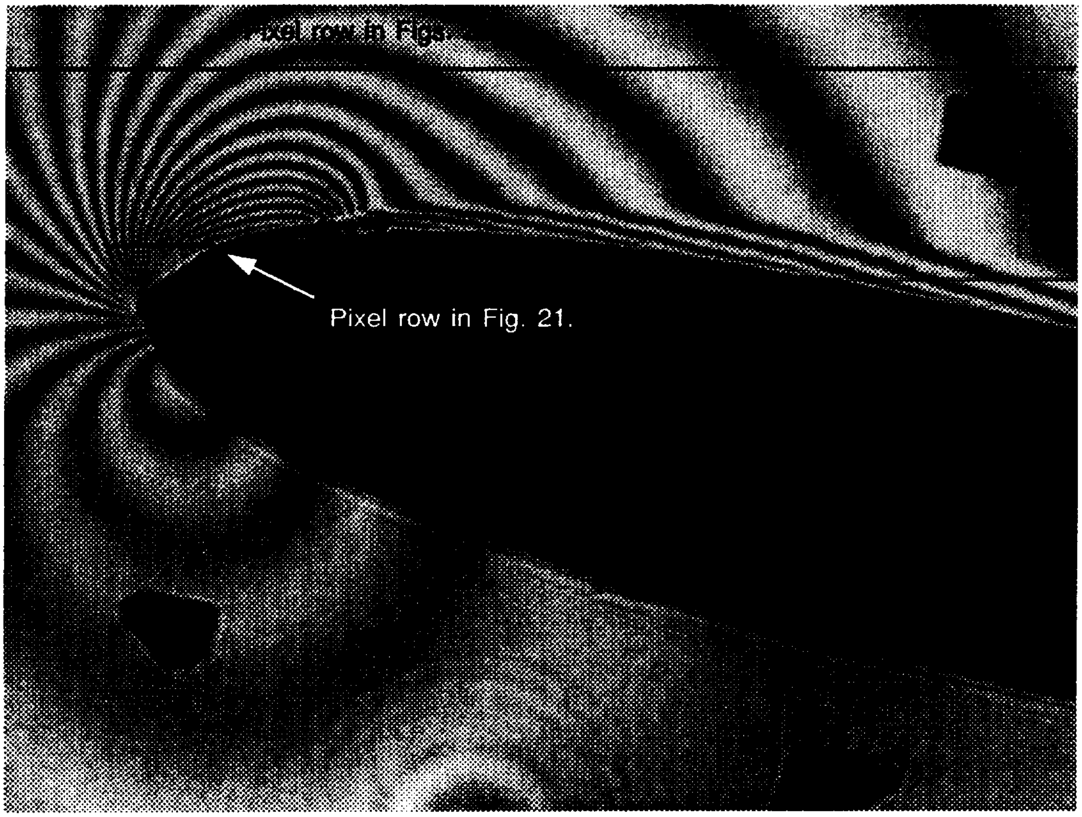

Fig. 19. Digitized PDI Image. Highlights Indicate Sources of Data Used in Subsequent Illustrations.

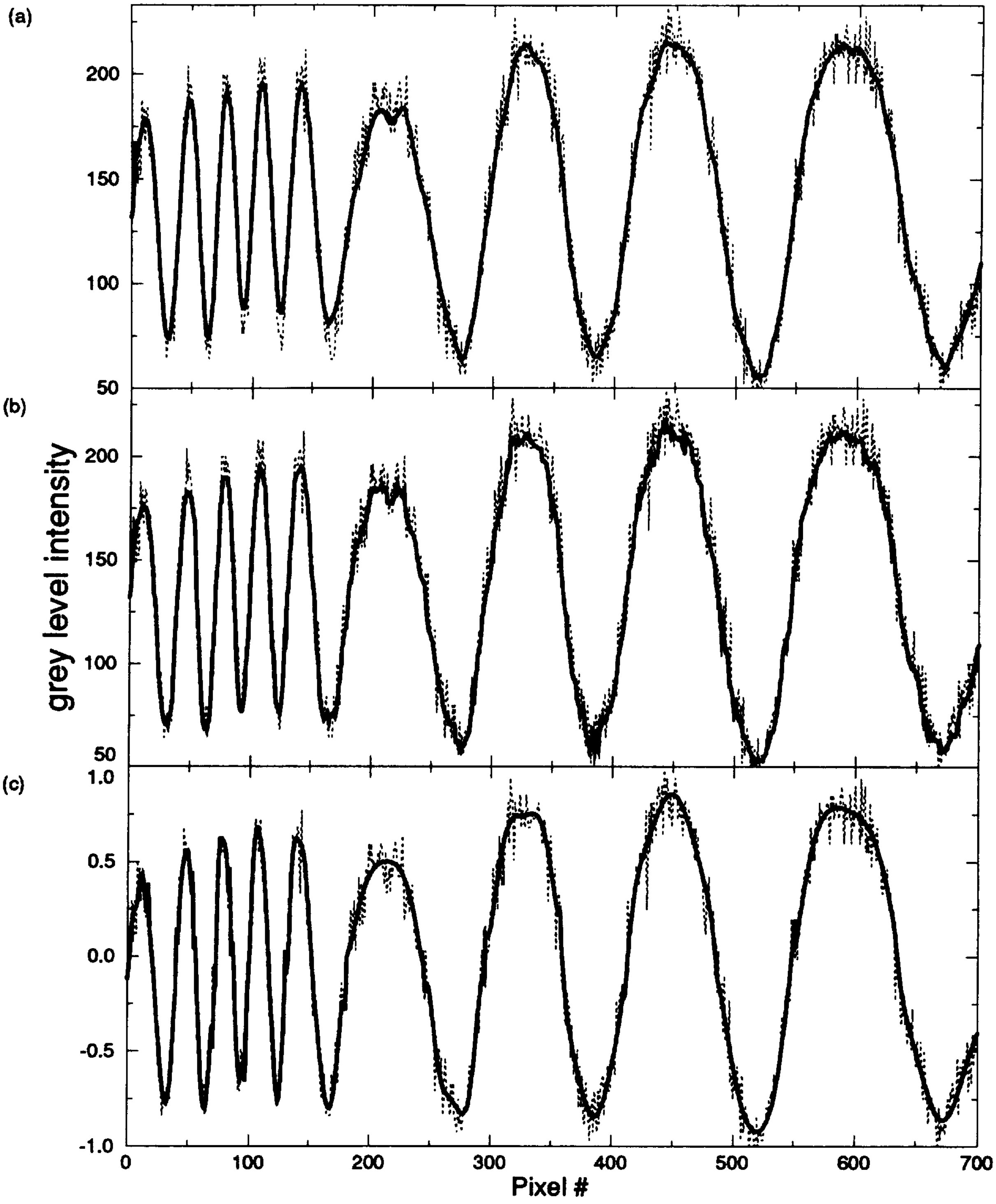

Fig. 20. Results of Low–Pass Filtering of Wide Fringes: (a) Seven Pixel Moving Window Average, (b) Spin Filter with Seven Pixel Mask, (c) Smoothing with Chebyshev Polynomial Approximation. ·········· Data from Row Highlighted on Fig. 19; ▬▬▬ Filtered Data.

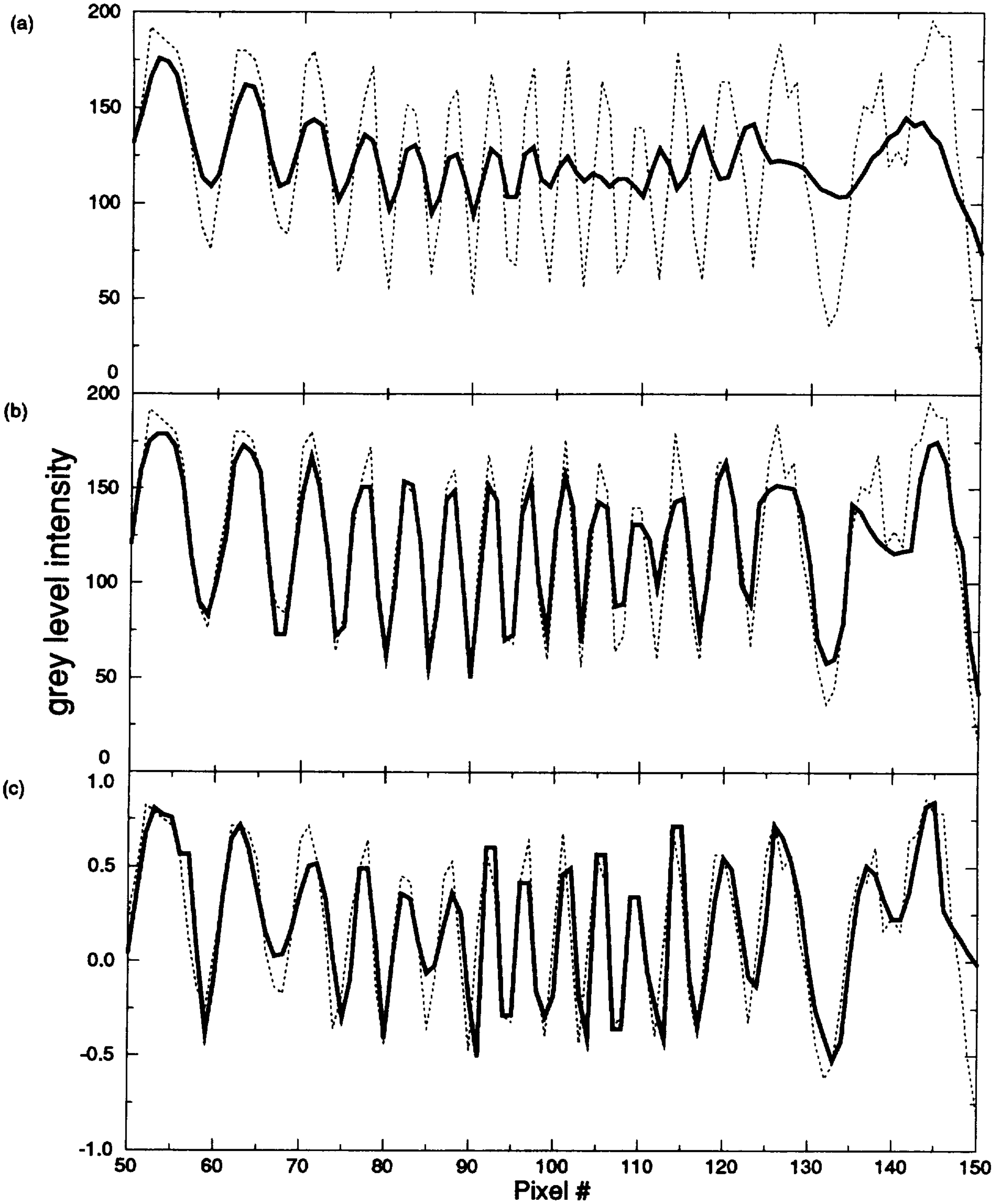

Fig. 21. Results of Low-Pass Filtering of Narrow Fringes: (a) Seven Pixel Moving Window Average, (b) Spin Filter with Seven Pixel Mask, (c) Smoothing with Chebyshev Polynomial Approximation. ········· Data from Row Highlighted on Fig. 19; ——— Filtered Data.

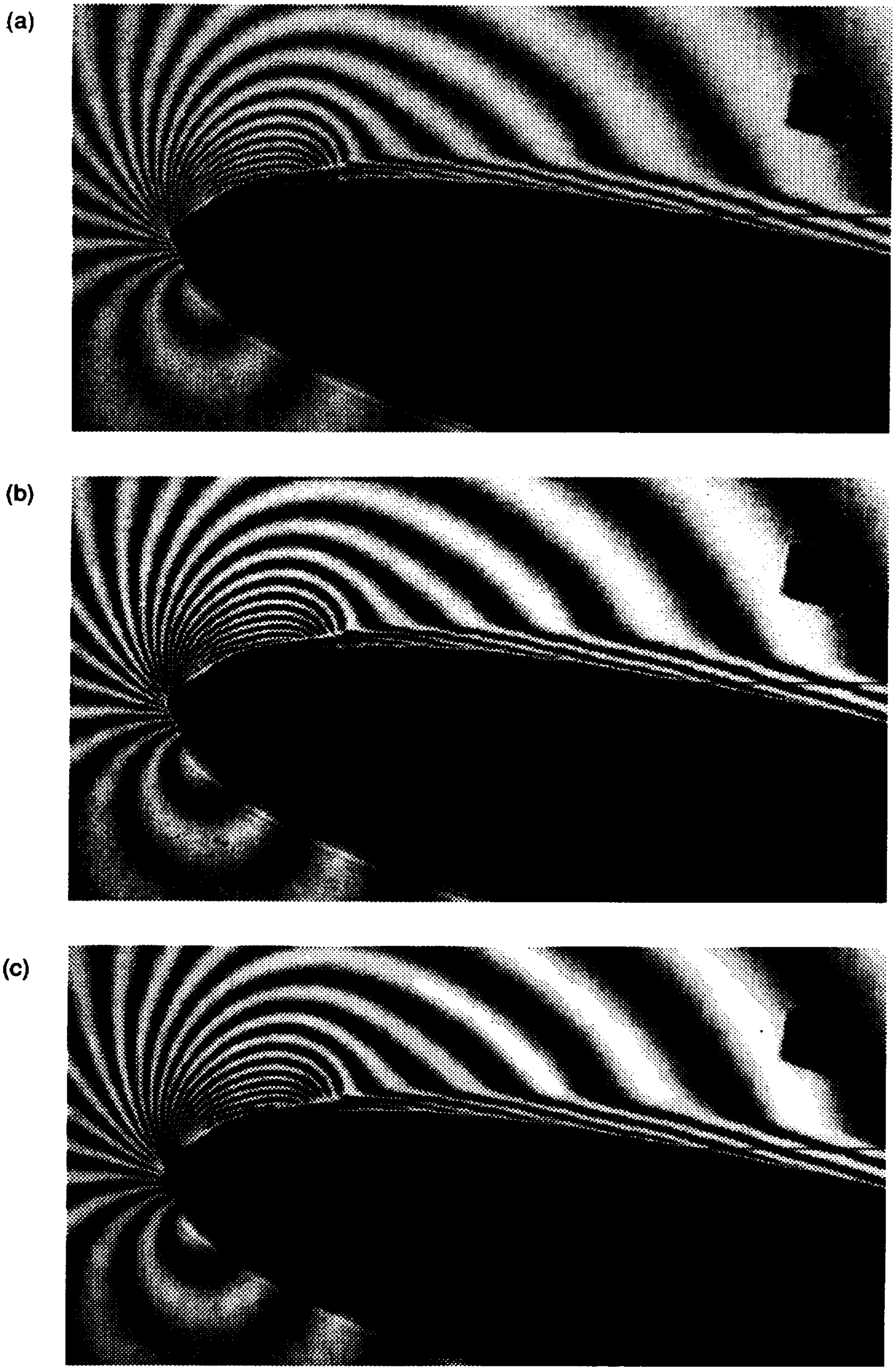

Fig. 22. Results of Image Enhancement and Filtering: $M = 0.3$; $k = 0.05$; $\alpha = 10^{\circ}$. (a) Digitized Image, (b) Image Enhanced by Global Histogram Equalization, (c) Enhanced Image Smoothed by Iterative Application of Spin Filter Using Seven Pixel Mask and Five Iterations.

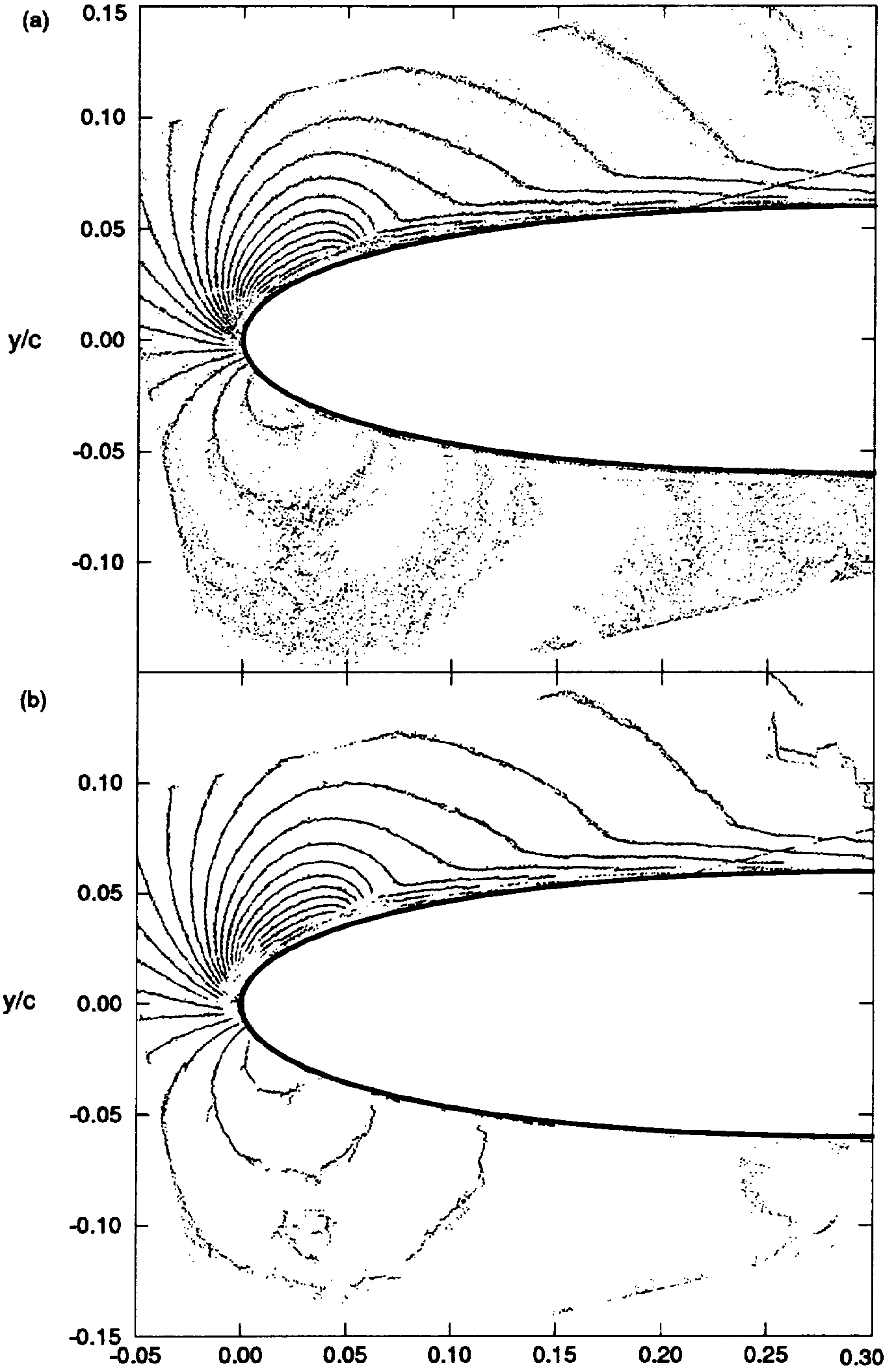

Fig. 23. Dark Fringe Centerlines Traced by Automatic Algorithm: M = 0.3; k = 0.05; α = 10°; Plotted in Body-Fixed Coordinates. (a) Tracing from Image Shown in Fig. 22b, (b) Tracing from Image Shown in Fig. 22c.

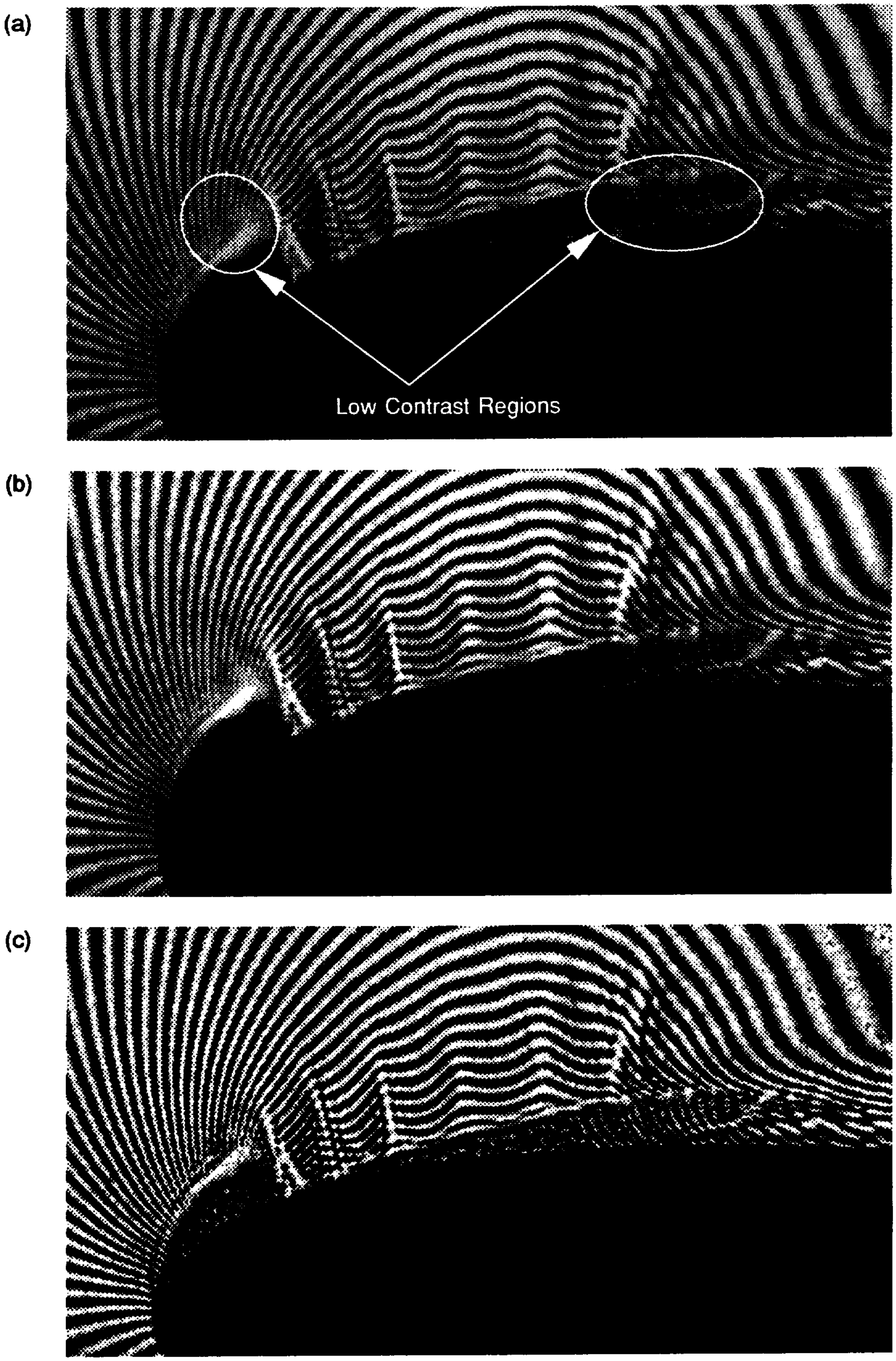

Fig. 24. Results of Image Enhancement: $M = 0.45$; $k = 0.05$; $\alpha = 10^{\circ}$. (a) Digitized Image, (b) Image Enhanced by Global Histogram Equalization, (c) Image Enhanced by Local Histogram Equalization Using a 15x15 Pixel Mask.

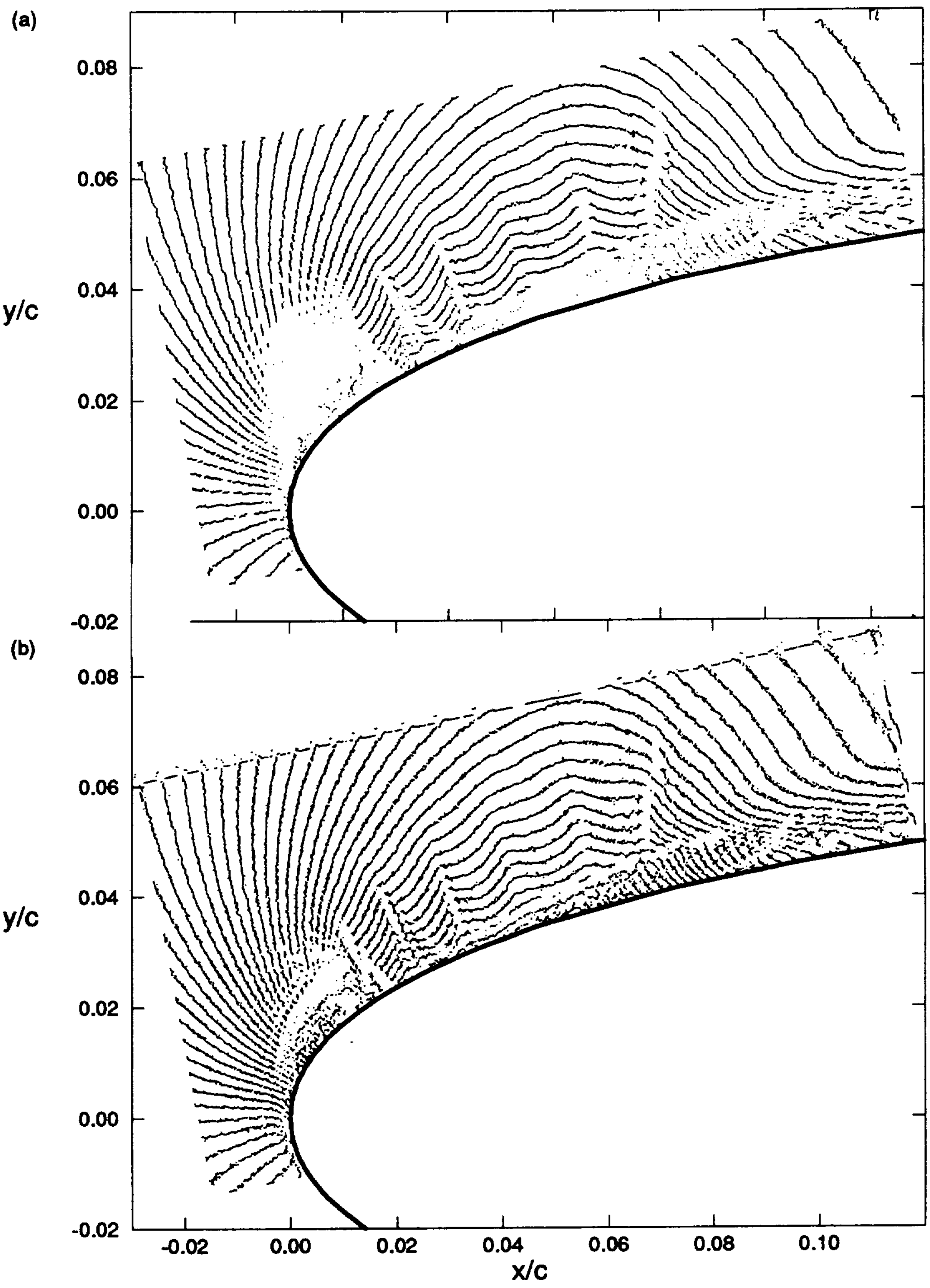

Fig. 25. Dark Fringe Centerlines Traced by Automatic Algorithm: $M = 0.45$; $k = 0.05$; $\alpha = 10^{o}$; Plotted in Body-Fixed Coordinates. (a) Tracing from Image Shown in Fig. 24b, (b) Tracing from Image Shown in Fig. 24c.